Subspace features and statistical indicators for neural network-based damage detection

Subspace features and statistical indicators for neural network-based damage detection

Marco Martino Rosso[a], Angelo Aloisio[b,*], Giansalvo Cirrincione[c], Giuseppe Carlo Marano[a,d]

[a] *Politecnico di Torino, DISEG, Department of Structural, Geotechnical and Building Engineering, Corso Duca Degli Abruzzi, 24, Turin, 10128, Italy*
[b] *Civil Environmental and Architectural Engineering Department, Università degli Studi dell'Aquila, via Giovanni Gronchi n.18, L'Aquila, 67100, Italy*
[c] *University of Picardie Jules Verne, Lab. LTI, Le Bailly, Amiens, Amiens, 80025, France*
[d] *Fuzhou University, College of Civil Engineering, Fuzhou, 350108, China*

Abstract

The late opportunities prompted by artificial intelligence have motivated the current research about structural damage detection strategies based on damage-sensitive subspace-based indicators (DI). Precisely, three different methodologies (A), (B), and (C) are discussed for multiclass damage classification with a multi-layer perceptron (MLP) network. Specifically, the network's inputs combine vibration response statistics with subspace-based features. Method (A) relies on statistical features only, whereas method (B) also considers the most informative subspace-based DI, retrieved from an empirical sensitivity analysis. Finally, method (C) provides a new perspective by overcoming the arbitrary choice of parameters affecting the subspace-based DIs computation. These three methods are tested on a numerical benchmark problem, and the results emphasize the last approach as the most promising methodology. For the sake of further validation purposes, the three methods have been finally tested on an experimental steel I-beam setup, evidencing the effectiveness of informative subspace-based DIs.

Keywords: structural health monitoring, operational modal analysis, subspace-based damage indicators, deep learning, multi layer perceptron

*Corresponding author.
Email address: angelo.aloisio1@univaq.it (Angelo Aloisio)

1. Introduction

Structural health monitoring (SHM) is nowadays one of the most relevant issues related to the public safety of transport systems, which concern the scientific community, public administrations and highway concessionaires [1, 2, 3, 4, 5, 6, 7]. Consequently, innovative techniques have been developed in recent years to better support a decision-making process, optimized maintenance programs and interventions to increase the nominal life of existing heritage [8, 9, 10, 11, 12, 13, 14]. In the SHM field, it is possible to distinguish at least two main categories of techniques. The former is denoted as parametric, usually based on analytical time-domain regression models [15, 16]. The latter includes non-parametric methods, which instead are not based on a model but rely on statistical treatments of the data [17], even allowing a quick insight into the information inside them [18]. One of the most widespread approaches for the dynamic behavior identification of a structural system is the operational modal analysis (OMA) [19, 20, 21].

The OMA comprises output-only post-processing techniques of the vibration response for estimating the natural frequencies and modal shapes. Among the most used algorithms in OMA, there are the Enhanced Frequency Domain Decomposition (EFDD) [22] and the Stochastic Subspace Identification algorithm (SSI) [23]. Nowadays, the EFDD method, which is a non-parametric, frequency domain procedure, and covariance-based SSI (SSI-cov), which is a parametric, time-domain procedure, are the most widespread techniques for OMA [18]. The SHM problem presents at least five levels of analysis as illustrated in [24, 18, 25, 26]: Level 1, associated with the initial damage detection phase; Level 2, damage localization phase; Level 3, identification of the type of damage; Level 4, quantification of damage severity; Level 5, related to the prediction of the actual remaining service life concerning the nominal one. The first four levels are associated with the well-acknowledged diagnosis phase [27], whereas the last one is related to the prognosis phase [24].

The present study discusses an example of Level 1 of the SHM problem. Theoretically, the damage detection task could be performed by monitoring any change in the experimental modal parameters. However, several researchers proved that these parameters obtained from the OMA are not the most informative elements to solve the Level 1 of SHM effectively [28, 29, 30].

Therefore, some other studies provided some most informative damage indicators (DIs) which do not strictly require OMA. [31] discusses at least two main advantages of adopting non-parametric damage detection procedures. They avoid manipulating vibration data, and, thus, no modeling errors are further introduced. Additionally, they could be easily integrated into automated monitoring systems. In particular, some of these DIs denoted as subspace-based [32, 33, 34], rely on residues calculated by covariance changes between two different situations: an initial reference condition and a current, possibly damaged, one [35]. Despite the excitation covariance may be significantly different among the two acquisition moments, these indicators are quite robust because they rely on the simple orthonormal factorization property among different subspaces, i.e. the active space in the reference state and the null space in the current situation [31]. Their robustness bestows them the capacity to effectively detect damages and not variations due to very different excitation inputs. In [36], they even adopt the subspace-based DI to perform the damage localization, Level 2 of an ideal SHM procedure.

The current study attempts to provide a novel framework for the damage detection task by adopting machine-learning artificial neural networks (ANN) models combined with the above-mentioned subspace-based DIs. Some previous attempts have been conducted by [37], in which a multi-layer perceptron (MLP) has been adopted in a supervised learning scheme combined with subspace DIs to perform classification task among a healthy and two other damage states. Despite their promising results, they evidence how the main subspace-based DIs drawback is related to the arbitrary choice of the time shift considered in the construction of the Hankel matrix and the truncation order to define the active and spaces, to detect damage and not the excitation variation noise effectively. In this paper, the authors have also provided a specific dataset collection to remove the arbitrary choice of the time shift and the truncation order, to improve further the damage classification performance of a relatively similar MLP architecture. In [38], both a support vector machine model and an MLP architecture have been trained on a numerical pinned-pinned beam model to perform the damage classification task. The ANN has been trained on statistical parameters directly calculated on the raw time series vibration data. This study has potential because the scholars adopted very elementary calculations without modeling assumptions associated with additional data manipulation. However, this method resulted in relatively poor accuracy on the simple numerical beam scheme, whereas accuracy negligibly improved on the analyzed real case studies.

In the present work, the authors attempt to further enhance this MLP scheme by giving as input both the most important statistical features and even considering a subspace-based DI [39]. Since this latter seems to be more sensitive to damage to the naive statistical indicators, their combination is expected to provide relatively higher accuracy in the classification performance. The proposed improvements to the damage detection framework with ANN and subspace-based DI are applied to a numerical simply supported beam. In addition, this simple benchmark discusses the sensitivity of subspace-based indicators to their input parameters. Furthermore, to validate the methods in a real-world case study, the authors tested the three methodologies on an experimental steel I-beam setup. To the authors' knowledge, no scholar carried out this study on subspace-based ANN damage detection before. The novel contributions of this article can be summarized as follows:

- The performance of three sets of DIs have been compared using ANN capabilities to solve multi-class damage classification. The goal is to assess the enhancement of the ANN classification performance, by including as input both statistical features estimated on raw vibration data and subspace-based indicators;
- A sensitivity analysis on the input parameters of the subspace-based indicators revealed the significance of their arbitrary choice and supported the development of a third set of DI;
- The third set of DIs considers as input of an ANN a class of subspace-based DIs in the attempt of removing the arbitrary user's choice of the parameters which significantly affected their calculations.
- An experimental laboratory test has been conducted on a steel I-beam to validate the effectiveness of the three proposed methodologies.

The current document is organized as follows. In Section 2.1, the theoretical basis of subspace-based DIs is briefly presented. Section 2.2 illustrates in detail the three proposed ANN-based methodologies denoted as (A), (B), and (C) for multiclass damage classification that combines statistical features and subspace-based DIs. Section 3 presents the analyzed benchmark numerical beam model case study. In Section 3.3 an empirical sensitivity analysis has been conducted to explore the impact of some hyperparameters on the damage identification process and the calculation of subspace-based DIs. In

Section 3.4, the MLP architecture for the numerical benchmark problem is described with the feature datasets arrangement for methods (A), (B), and (C), and the training results are presented. Section 4 illustrates an experimental laboratory test conducted on a steel I-beam to validate the effectiveness of the three proposed methodologies. Finally, Section 3.5 extensively discusses the classification results and the effectiveness of the three proposed methodologies in the analyzed case studies.

2. Damage detection with subspace-based artificial neural networks

2.1. Brief overview of subspace-based damage indicators

In the last decades, many different damage diagnosis approaches based on OMA techniques have been proposed, relying on the extraction of some damage-sensitive features from output-only vibration data [40, 41]. Generally, the feature vector is approximately assumed as zero mean normal Gaussian distributed in the reference state (assumed as an undamaged situation) which evolves in a non-zero mean when damages occur. Therefore, a residual vector may allow monitoring of the relative changes among the new probable damaged state, and the initial reference one [42]. Some residuals definitions have been proposed in the literature, e.g. the subspace-based residual [43], the transfer matrix-based residual [44], residuals built on a null-space based comparison of data Hankel matrices [45], on the difference of output covariance Hankel matrices [46] or directly on the modal parameter differences [47].

The present study mainly focused on the subspace-based residuals approach which has its roots in the SSI-cov identification algorithm [23]. The subspace residuals are classified in *conventional* and *robust* with respect to how they are influenced by noise and changes in input excitation patterns [43]. The residual matrix relies on the orthonormal property between the subspaces related to a reference situation in comparison with the subspace related to a different structural response dataset, which could be varied because of input noises or structural damages. The main advantage of the subspace-based DIs is related to the fact that they do not strictly require the identification process of the structure. For example, in [48, 49], a residual function was proposed to detect changes in the intrinsic dynamic properties directly from raw measurements (e.g. acceleration responses), without performing structural modal identification in the damaged state. Denoting vibration measured data as $(\boldsymbol{y}_k)_{k=1,\dots,N}$, a consistent estimate of the the

theoretic block Hankel matrix $\hat{H}_{p+1,q}$ is obtained from the empirical output covariances [50]

$$\hat{R}_i = \frac{1}{N}\sum_{k=1}^{N} y_k y_{k-i}^T \quad \Rightarrow \quad \hat{H}_{p+1,q} = \begin{bmatrix} \hat{R}_1 & \hat{R}_2 & \dots & \hat{R}_q \\ \hat{R}_2 & \hat{R}_3 & \dots & \hat{R}_{q+1} \\ \vdots & \vdots & \ddots & \vdots \\ \hat{R}_{p+1} & \hat{R}_{p+2} & \dots & \hat{R}_{p+q} \end{bmatrix} \tag{1}$$

[48, 49] originally proposed a residual function comparing modal parameters between a reference (undamaged) state and a current (damaged) one. However, [51] proposed a non-parametric damage detection approach without requiring carrying out the complete modal identification in the reference state. In SSI-cov algorithm, the modal identification procedure is mainly based on the singular value (SV) decomposition of the Hankel matrix [18, 45]

$$\hat{H}_{p+1,q} \approx [\boldsymbol{U}_1 \boldsymbol{U}_2] \begin{bmatrix} \boldsymbol{S}_1 & \boldsymbol{0} \\ \boldsymbol{0} & \boldsymbol{0} \end{bmatrix} [\boldsymbol{V}_1 \boldsymbol{V}_2]^T \approx \boldsymbol{U}_1 \boldsymbol{S}_1 \boldsymbol{V}_1 \tag{2}$$

where $\boldsymbol{U}_1$ represents the left active subspace of the independent column vectors of the Hankel matrix, $\boldsymbol{U}_2$ denotes the null subspace, similar definitions are provided for $\boldsymbol{V}_1$ and $\boldsymbol{V}_2$ for row vectors of Hankel matrix, and $\boldsymbol{S}_1$ collects the sorted non-negligible SVs in a diagonal matrix. The orthonormal properties of these matrices state that

$$\hat{H}_{p+1,q} \boldsymbol{V}_2 \approx \boldsymbol{\epsilon}_V \quad , \quad \boldsymbol{U}_2^T \hat{H}_{p+1,q} \approx \boldsymbol{\epsilon}_U \tag{3}$$

The above residues $\boldsymbol{\epsilon}_V$ and $\boldsymbol{\epsilon}_U$ can be different from zero vectors because of noise effect or neglected weakly excited high modes. However, [45] pointed out that they are not the ideal candidates for tracking relative changes for damage detection purposes, taking into account the same state. Indeed, the amplitude of the residues, resulting from the erroneous definition of the system order or the amplitude excitation, may mask the residues variation due to small structural damages. Instead, the above orthonormal property can be exploited by comparing two different states. Therefore, the conventional residue can be expressed as the product of an empirical (non-parametric) null subspace $\boldsymbol{U}_{2,\text{ref}}$ in the reference state and the Hankel matrix $\hat{H}_{p+1,q,\text{cur}}$ in

the current state [48, 49]:

$$\hat{\boldsymbol{\epsilon}}_c = \boldsymbol{U}_{2,\text{ref}}^T \hat{H}_{p+1,q,\text{cur}} \tag{4}$$

However, the excitation covariance may vary between different measurement sessions of the system because of random environmental factors. Therefore, [43, 45] presented a new residue definition robust to variations of excitation, considering the product of the null subspace $\boldsymbol{U}_{2,\text{ref}}$ in the reference state and the active subspace $\boldsymbol{U}_{1,\text{cur}}$ in the current state:

$$\hat{\boldsymbol{\epsilon}}_r = \boldsymbol{U}_{2,\text{ref}}^T \boldsymbol{U}_{1,\text{cur}} \tag{5}$$

In [45], the authors have provided a geometrical interpretation of the residue matrix concept, such as the expression of a loss of orthonormality between reference subspace and another current state. Therefore, they give some DIs related to the rotation angle which arises between the two subspaces when structural damage occurs. Despite different possible DIs formulations have been provided [48, 52], in this study the authors referred to Yan et al. [45], in which the DI has been established as the spectral norm of the conventional or robust residue matrix:

$$DI_{c,\text{Yan}} = \text{norm}(\hat{\boldsymbol{\epsilon}}_c) \quad , \quad DI_{r,\text{Yan}} = \text{norm}(\hat{\boldsymbol{\epsilon}}_r) \tag{6}$$

where $\text{norm}(\cdot) : \mathbb{R}^{m \times n} \rightarrow \mathbb{R}$ is the matrix spectral norm operator, i.e. the maximum SV. In the current study, the Yan's et al. [45] $DI_{r,\text{Yan}}$ has been selected as a subspace-based damage-sensitive feature to train the ANN classification models presented in Figure 1.

2.2. Proposed neural network-based damage detection methodologies

To evaluate the health state of a specific structure with a monitoring system, nowadays, a widespread approach relies on the dynamic identification of the structure using output-only vibration data. A new methodology is presented in the current study based on integrating the ANN into the damage identification process. To leverage at most all the potentialities of artificial intelligence techniques, particular care must be dedicated to the dataset collection, which plays a crucial role in determining accurate and reliable final results. Therefore, after placing the accelerometer sensors on the structure under investigation, the first critical phase is collecting output-only vibration data response. Specifically, as discussed in the previous section, the subspace-

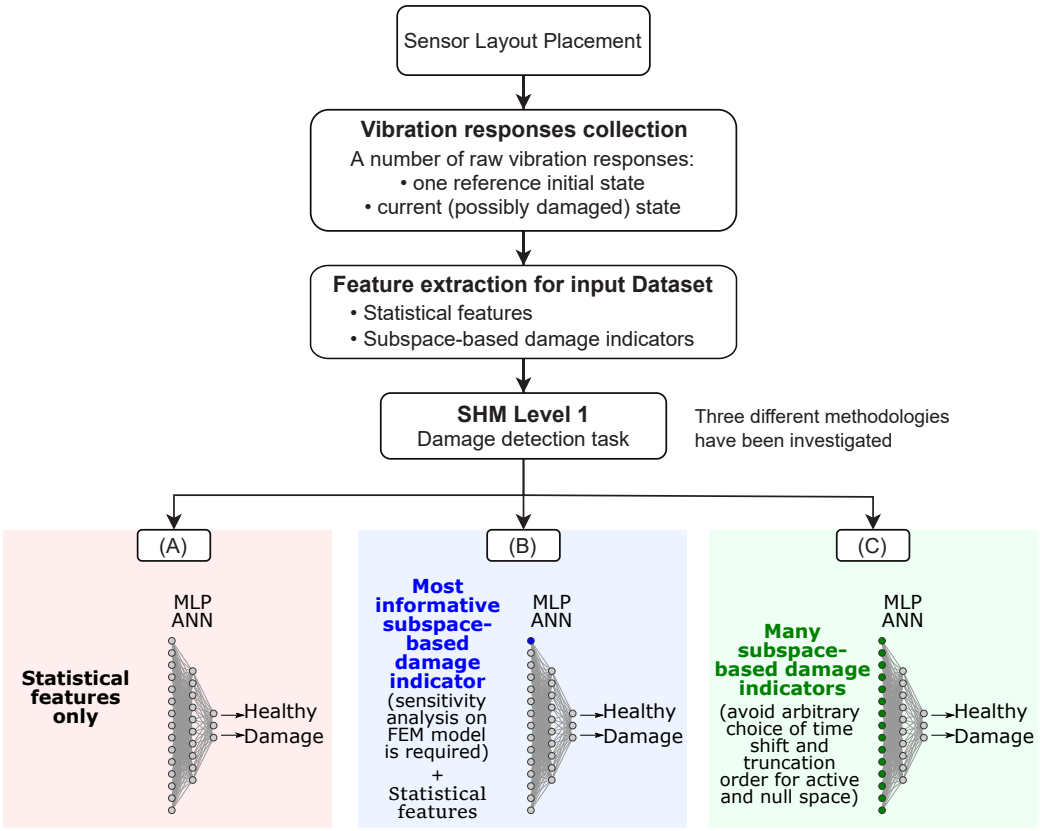

Figure 1: Flowchart of the three ANN-based damage detection proposed methods.

based damage indicators rely on comparing two different states. Indeed, the very first measurement session is assumed as the reference state. On the other hand, any subsequent measurement session should be considered as a current state (undamaged or potentially damaged). Since the availability of real-world recorded data may be strongly limited in general, the current method relies on a data augmentation procedure based on numerical simulations. Specifically, a finite element (FE) model calibrated on the reference state measurements may be dynamically excited imposing various damage conditions in order to collect a sufficiently comprehensive dataset of vibration responses related to different and likely damaged current states.

After collecting these structural responses dataset, three different methodologies respectively named (A), (B), and (C) have been developed in the current research study, as schematically illustrated in Figure 1. Precisely,

these three methods share a common artificial intelligence core, i.e. an ANN model with a MLP architecture typology. A classification task is entrusted to the neural model with the final goal of recognizing the health status of the current state of the structure under investigation. Nevertheless, to fulfill this task, the authors have identified three possible different sets of input features to feed the MLP model, thus formalizing three different methodologies.

Inspired by the previous study of Finotti et al. [38], method (A) involves a supervised damage classification task based on statistical features only. Specifically, some basic statistics have been computed directly on the raw time-histories vibration data. These descriptors, e.g. sample mean, sample variance, mean square, root mean square, etc., are used to feed the MLP model since they represent potentially time-domain discriminating features between the undamaged reference state and a damaged current state. In particular, as demonstrated in [38], in the current study, only the following most significant and discriminative statistical features have been considered, i.e. equations (7a)-(7f). Denoting the acceleration time series recordings with n_a components as $\boldsymbol{x}$, the extracted statistical features taken into consideration are the peak value $x_{\mathrm{P},(i,j)}$, the mean square value $x_{\mathrm{MS},(i,j)}$, the root mean square $x_{\mathrm{RMS},(i,j)}$, the variance $x_{\mathrm{VAR}(i,j)}$, the standard deviation $x_{\mathrm{STD},(i,j)}$ and the K-factor $x_{\mathrm{K},(i,j)}$.

$$x_{\mathrm{P},(i,j)} = \max\{|x_k|\}_{k=1}^{n}, \tag{7a}$$

$$x_{\mathrm{MS},(i,j)} = \frac{1}{n}\sum_{k=1}^{n} x_k^2, \tag{7b}$$

$$x_{\mathrm{RMS},(i,j)} = \sqrt{\frac{1}{n}\sum_{i=1}^{n} x_k^2}, \tag{7c}$$

$$x_{\mathrm{VAR}(i,j)} = \frac{1}{n}\sum_{k=1}^{n}(x_k - \overline{x})^2, \tag{7d}$$

$$x_{\mathrm{STD},(i,j)} = \sqrt{\frac{1}{n}\sum_{k=1}^{n}(x_k - \overline{x})^2}, \tag{7e}$$

$$x_{\mathrm{K},(i,j)} = x_{\mathrm{P},(i,j)} \cdot x_{\mathrm{RMS},(i,j)}. \tag{7f}$$

In the previous equations, j denotes the numbering of the j-th sensor placed on the structure, whereas i refer to the i-th current, potentially damaged,

state under consideration. Nonetheless, despite the promising idea of method (A), in [38] the accuracy classification performance was demonstrated being decent but outstanding. The reasons may be probably lie in the limited scattering interval of some statistics even though passing from an healthy status to a very seriously damaged one.

Therefore, the latter consideration motivated the authors to attempt further improving method (A) thus investigating another set of more discriminative input features. As illustrated in Figure 1, method (B) plans to feed the MLP network with the previous statistical features jointly with a most discriminative Yan's et al. [45] subspace-based damage-sensitive feature $DI_{r,\mathrm{Yan}}$, see equation (6). According to the brief recall of the background theory presented in the previous section, the calculation of this indicator requires an arbitrary user's choice about at least two parameters, i.e. the time shift and the truncation order, which in turn defines the active and null subspace dimensions. Therefore, a possible more reliable and systematic method to define the most informative, and thus the most discriminative subspace-based feature, can be handled with an empirical sensitivity analysis. The final aim of the latter is to detect the optimal combination of these two governing parameters in order to achieve the most damage-sensitive subspace-based indicator. However, this kind of analysis may be sometimes quite tricky, depending on the specific modal identification problem, and rather computationally expensive. Nevertheless, a certain degree of arbitrary still remains within the choice of these two governing parameters.

Consequently, a third method (C) has been proposed by the authors in the current study, as illustrated in Figure 1. In this latter case, the MLP network has been fed with a set of input features entirely represented by the solely Yan's et al. [45] subspace-based damage-sensitive features $DI_{r,\mathrm{Yan}}$, see equation (6). The objective of method (C) is thus removing the remaining user's arbitrary degree in the choice of the governing parameters affecting the computation of the subspace-based indicators, i.e. the time shift and the truncation order. Indeed, an entire set of Yan's et al. DIs only can be computed by varying both the time shift and the truncation order values within certain reasonable intervals respectively. Each time shift and truncation order pair determines a specific Yan's et al. DI value. In this way, in addition to the advantage of reducing the arbitrary level of the previously proposed methods, method (C) allows considering those hidden patterns of the various subspace-based indicators given by the governing parameters for the same raw time series. Moreover, this third method is expected to be as-

sociated with a higher classification accuracy due to the higher sensitivity of these indicators to structural damages.

In summary, with method (A) the MLP network gets as input some time-domain sample statistical features only, calculated on the output-only vibration response signals collected from the structural system under study. In order to improve the performance of method (A), with method (B) a more informative subspace-based DI has been added to the feature vector composed of the statistical features. In general, at least two hyperparameters need to be defined in advance to calculate the subspace-based DI, i.e. the time shift parameter and the truncating order, which in turn determines the active subspace dimensions, or complementary, the null one. A proper combination of these governing parameters may provide the most informative subspace-based DI, and thus the most discriminative for pattern recognition methods like the ANNs. For this aim, a sensitivity analysis is usually required. Eventually, with the third method (C), the input feature vector to the MLP network has been set as an ensemble of various subspace-based DIs. This set of features is calculated for the same time series by varying the values of the two required governing hyperparameters, i.e. the time shift and the truncation order, in an attempt of removing the arbitrary choice of these hyperparameters and avoid a sensitivity analysis beforehand, which can be substantially laborious. The three currently proposed methodologies have been tested firstly on a numerical benchmark problem and further validated on an experimental setup, as hereinafter discussed.

3. Application of the proposed methods to a numerical case study

The above-mentioned proposed methodologies have been tested and validated firstly on a numerical case study, and afterward on an experimental steel I-beam setup. In the following paragraphs, an extended description of the adopted numerical case study is discussed. Furthermore, the traditional dynamic identification approach through modal analysis and OMA has been carried on, highlighting the limitations of the current conventional approaches.

3.1. Numerical Beam Model and traditional modal analysis

In the current study, an initial numerical beam model has been considered. The structural system, depicted in Figure 2, has been implemented through the *OpenSeesPy* module [53]. This latter allows leveraging all the

advantages and powerful capabilities of the open-source OpenSees finite element (FE) software controlled by a Python interpreter instead of the traditional Tool command language (Tlc) approach [53]. The numerical case study is a simply supported steel beam modeled with *elasticBeamColumn* elements, with a square cross-section of side 0,10 m and a span length of 2,00 m. Figure 2 illustrates its geometry, in which x, y, z denotes the Cartesian coordinates reference system, b is the square cross-section side, L is the span length, g_{k1} is the self weight load which produce the static deflection $v(z)$. A Gaussian white noise acceleration input ($\ddot{u}_y(t)$) is adopted as dynamic input to the simply supported beam. The steel material implemented

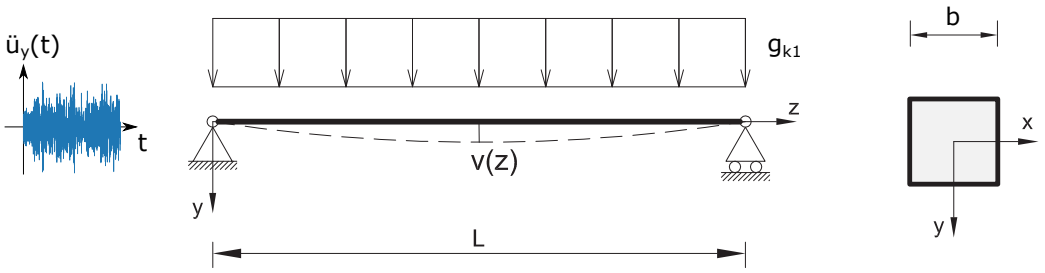

Figure 2: Simply supported numerical beam geometry illustration.

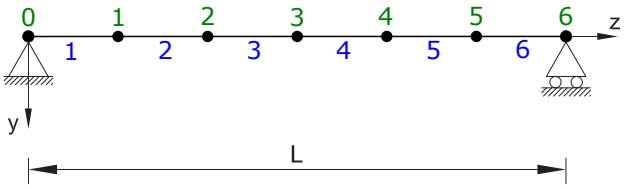

(a)

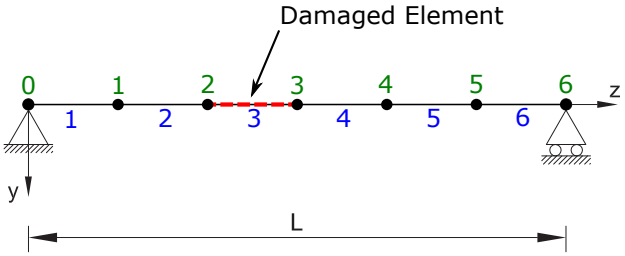

(b)

Figure 3: Numerical beam FEM with element (blue) and node (green) numbering. (a) undamaged model; (b) example of damaged model.

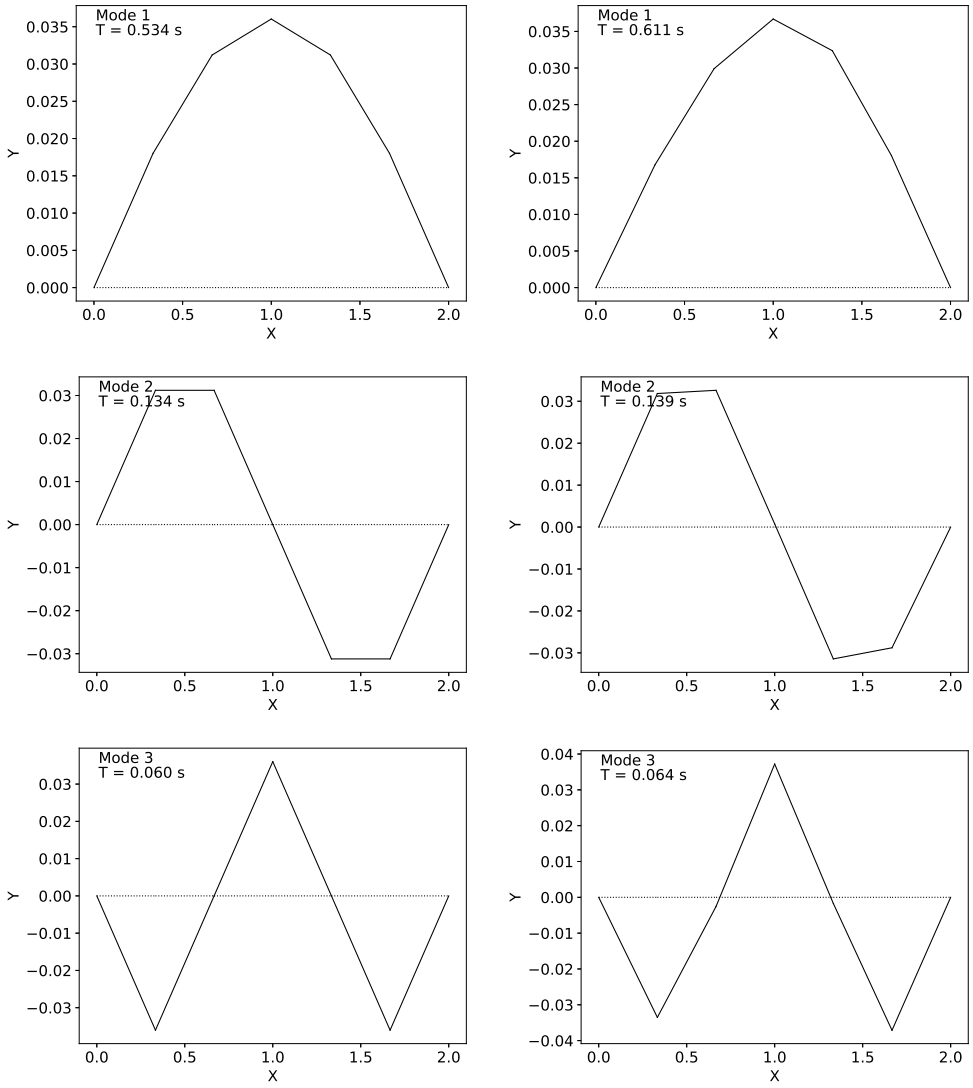

Figure 4: On the Left, undamaged beam normalized mode shapes; on the right, damaged beam normalized mode shapes referred to the damaged case illustrated in Figure 3.

as *uniaxialMaterial* is characterized by Young's modulus $E = 210$ GPa and a mass density of $\rho = 7850\ \mathrm{kg/m^3}$. One beam support was dynamically excited by a vertical Gaussian random white noise acceleration [31]. This approach is well-acknowledged in the scientific literature to simulate the unknown environmental dynamic excitation, and operational conditions in nu-

Table 1: Comparison of the natural period and natural frequency in the undamaged case and the damaged one.

	Undamaged Case		**Damaged Case**	
Mode	**T [s]**	**f [Hz]**	**T [s]**	**f [Hz]**
1	0.534	1.872	0.611	1.638
2	0.134	7.479	0.139	7.184
3	0.060	16.722	0.064	15.680
4	0.049	20.583	0.052	19.368

Table 2: CrossMAC comparison between mode shapes retrieved from modal analysis undamaged and damaged beam model.

		Undamaged Case			
	Mode	**1**	**2**	**3**	**4**
Damaged Case	**1**	0.9987	0.4359	0.5800	0.6245
	2	0.3948	0.9993	0.4281	0.4838
	3	0.5906	0.4112	0.9981	0.9535
	4	0.5768	0.3837	0.8866	0.9616

merical cases or laboratory experiments [15, 54]. The white noise process has been generated by a random sampling of a standard zero-mean normal $N(0, 1)$, normalized, and rescaled up to 0.01 g of peak ground acceleration (PGA). The input acceleration has been imposed similarly to an earthquake excitation limited to the vertical direction only and in one single support to be sure to excite all modes. Theoretically, it would be more accurate to excite every mass independently in the beam nodes. However, any perturbation propagates almost instantaneously in every element of the beam due to the high elastic wave propagation velocity compared to the modal dynamics [55]. Furthermore, this straightforward approach does not compromise the overall convergence when solving the considered beam model.

As depicted in Figure 3, the beam element has been discretized with a uniform mesh, in which in each node the time history acceleration responses have been collected, simulating the presence of accelerometer sensors placed in correspondence with the FE nodes. Thereafter, in the damaged model, a severe damaging with cross-section reduction of 50% (symmetrically reduced along the local y-axis) has been considered in a specific fixed position , thus affecting the bending stiffness, as illustrated in Figure 3.

This specific case permitted the authors to develop a sensitivity analysis which is detailed in the next section. Beforehand, a modal analysis has been conducted in order to compare the mode changes in the damaged and

undamaged situation. Figure 4 and Table 1 highlight a general increase of the natural periods due to the presence of the damage concomitantly with the loss of symmetry in the mode shapes due to the non-symmetric damage. This is strongly related to the fact that the induced damage involves both the flexural stiffness properties and even a mass loss which influences the intrinsic dynamic properties.

In order to evaluate the similarity between the mode shapes in the damaged and undamaged case, the modal assurance criterion (MAC) may be adopted. This criterion is expressed as

$$\mathrm{MAC} = \frac{\left|\hat{\boldsymbol{\phi}}_1 \hat{\boldsymbol{\phi}}_2^T\right|^2}{\left|\hat{\boldsymbol{\phi}}_1\right|^2 \left|\hat{\boldsymbol{\phi}}_2\right|^2} \tag{8}$$

where $\hat{\boldsymbol{\phi}}_i$, given $i = 1, 2$, represents the estimated mode shape vector referred to damage and undamaged situations. Despite the MAC is usually adopted to give the correlation among the mode shapes, when it compares the similarity among different situations it is also denoted as *crossMAC*. After normalizing to [0,1] interval range the mode shapes, the crossMAC results have been reported in Table 2. Focusing on the main diagonal, it is worth noting a similarity of 99% among the first three mode shapes and it decreases to 96% on the fourth mode. On the other hand, focusing on all off-diagonal elements, the cross-correlations between different modes in the two different situations are not of major interest within the scope of the present study.

In conclusion, the traditional modal analysis is apparently still able to evidence the presence of damage, showing changes in natural frequencies of the structure in the two compared undamaged and damaged scenarios. Nonetheless, as stated in [56, 57, 58], conventional modal analysis techniques are suitable to identify reasonably separated modes, and often more sophisticated tools are required in presence of errors, uncertainties, or complex structural systems. Damage detection schemes solely based on conventional modal analysis with complex structures may be tough because any modeling error can strongly affect traditional modal analysis results. Furthermore, in real-life applications, noise naturally produces changes in mode shape, jeopardizing any damage detection trivially based on conventional modal analysis. Moreover, the traditional modal analysis alone requires knowing the damage type and location beforehand to create two accurate FEM reproducing the real sit-

uation, which are instead the final goals of any damage detection procedure. Therefore, damage detection methods based on modal information retrieved e.g. from OMA procedures have been developed in the last decades.

3.2. Operational Modal Analysis on collected output accelerations

The acceleration responses have been collected in the FE beam model nodes to simulate a realistic monitoring system. Afterward, an initial static analysis considering the self-weight deformed shape, and time histories analyses have been conducted through *OpenSeesPy* module considering a vertical acceleration history as input. Specifically, the random white noise sampled from a standard Gaussian distribution is characterized by a sampling frequency of 50 Hz. In contrast, the time history analyses have been conducted with a pseudo-time increment step of 0.002 s. This means that the collected acceleration histories response data are simulating a monitoring setup composed of accelerometers with a sampling frequency of 500Hz. Five-minute acquisition duration sessions have been performed on damaged and undamaged cases.

At first, these data have been employed to validate the numerical FE beam model through a traditional output-only dynamic identification process. Beforehand, data have been detrended and decimated to get better visualization results in the frequency range of interest 0-50 Hz, representing a reasonable range, based on previously modal analysis results. The two techniques adopted in the current study are the EFDD [59] and the SSI-cov [60]. These two techniques have been implemented in a Python module developed by the authors [61]. Figure 5 illustrates, on the left, the results

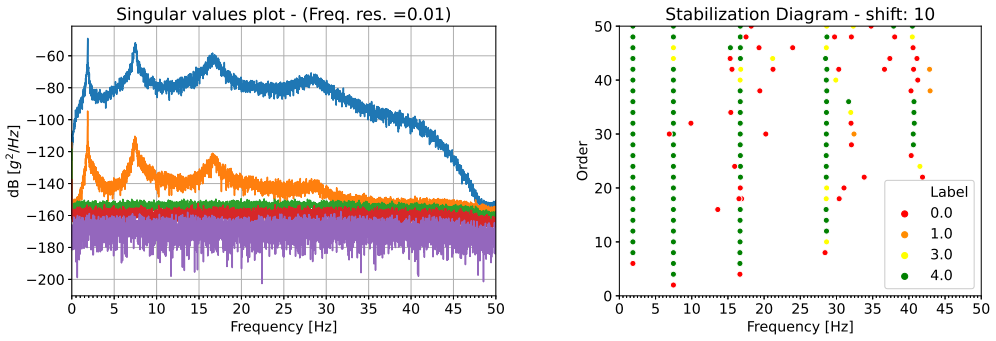

Figure 5: On the Left, EFDD results of the undamaged signals; on the right, SSI stabilization diagrams of the undamaged signals.

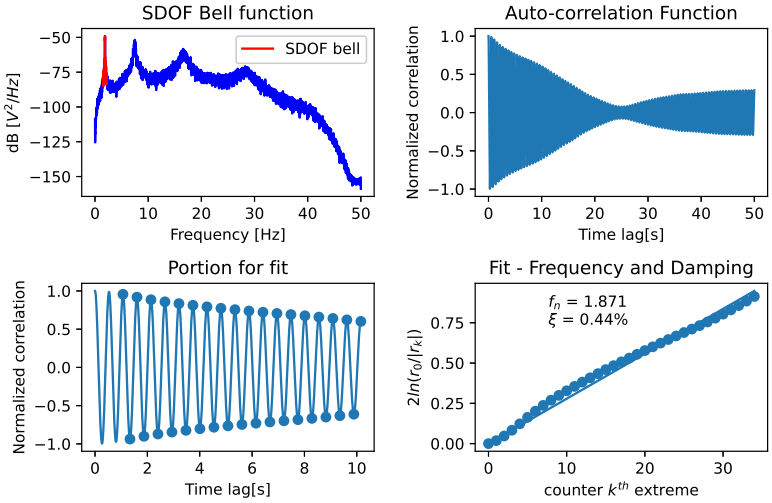

Figure 6: SDOF bell extraction and modal properties definition from EFDD algorithm related to the first natural frequency peak.

Table 3: OMA results on undamaged and damaged case.

Mode	Undamaged			Damaged		
	OMA		Modal An.	OMA		Modal An.
	f [Hz]	ξ [%]	f [Hz]	f [Hz]	ξ [%]	f [Hz]
1	1.871	0.44	1.872	1.635	0.30	1.638
2	7.501	1.46	7.479	7.163	1.44	7.184
3	16.440	3.71	16.722	15.854	3.12	15.680
4	28.031	3.69	20.583	26.451	2.32	19.368

of the EFDD algorithm, which shows the SV decomposition of the power spectral density (PSD) which allows detecting the natural frequencies by its resonance peaks [54]. Exploiting the MAC criterion, it is possible to extract a single degree of freedom SDOF bells around the peaks and find the modal properties for each resonance frequency, as depicted e.g. in Figure 6. Instead, Figure 5 illustrates, on the right, the stabilization diagram retrieved from SSI-cov algorithm, which allows identifying the modal properties from the stable poles' vertical alignments with increasing order of the model complexity. The colors of the poles in the stabilization diagram, identified by the numbers 0.0 to 4.0 in the legend, indicate respectively: unstable poles, stable in frequency, stable in frequency and mode shape, stable in frequency

and damping, stable in frequency damping and mode shape, accordingly to the poles stability checks [62, 63]. Finally, the traditional OMA results referred to the undamaged and the damaged situations are reported in Table 3, showing an overall acceptable agreement with modal analysis results and demonstrating the validation of the proposed numerical model as a realistic simulation of a monitoring setup.

3.3. Sensitivity of subspace-based indicators to time-shift, truncation order and time series duration

As explained in Section 2.1, Yan's et al. [45] DIs represent, among the others, an intuitive and interesting subspace-based damage-sensitive feature characterized by a geometrical interpretation. The main advantage of working with these indicators is that they do not require a prior OMA for dynamic structure identification. The current section focuses on sensitivity analysis to build a numerical dataset of damage-sensitive features that will consider many different damage situations and different white noise Gaussian random processes as input. The discussion allows defining the user's choice parameters to get the most informative subspace-based DI features. In particular, the influence of the choice of the active space dimension, and consequently the null space dimension, has been analyzed, combined with the entirely arbitrary user's selection of the time shift. As depicted in Figure 7, there is a great variation among the Yan et al. subspace-based DI with different choices of both active subspace dimension and time shift. Focusing on the first aspect, the active space dimension is related to the space whose base is represented by the left singular column vectors associated with the singular values which are quite different from zero. Since the singular values decomposition provides a diagonal matrix with singular values in ascending order, it is quite easy to evidence where there is a great relative difference between the first singular values and the last ones. As a matter of fact, a consistent discontinuous step between singular values and orders of magnitude has been recorded at the fifth singular value (passing from 10^{-6} to 10^{-16}). Nevertheless, Figure 7, demonstrated that, with a constant time shift, even with different subspace dimensions the Yan et al. DIs presented quite scattered values. Specifically, with an active space dimension equal to five which corresponds to the watershed among the DIs' order of magnitude, the Yan et al. DI does not provide any information.

On the other hand, regarding the choice of the time shift, this is related to the block rows considered in the block Toeplitz matrix assembling. According

to [18], for identification of a system of order n, the time shift, i.e. the number of block rows, i have to respect the condition: $li \geq n$, where l is the number of monitoring sensors applied on the structure. Since for practical applications on continuous systems, the n is theoretically infinite and, in practice, unknown, different rules of thumb and practical approaches have been proposed in the literature to identify a good choice for the time shift, often based on power spectral density matrix [18]. Trying to provide a quite concrete interpretation of this user-defined parameter, the longer the time shift is, the greater time window interdependencies will be considered in the correlation matrices of the raw data but in the face of a greater computational effort. Therefore, when dealing with SSI-cov, the time shift is chosen in an empirical way until e.g. the stabilization diagram provides a good resolution to a first-sight identification of the vertical alignments related to stable poles with progressively increasing system's order.

It is worth noting that Figure 7 pointed out that results related to active space dimension 1 were virtually the same as active space dimension 6, whereas results associated with dimension 2 were coincident with dimension

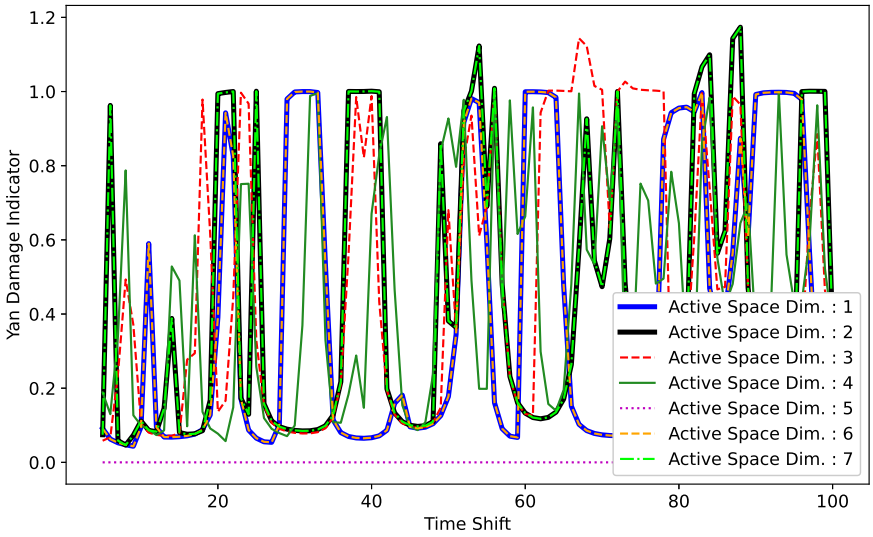

Figure 7: Sensitivity analysis on active space dimensions and, consequently the complementary null space dimensions, compared with the time shift user's defined choice.

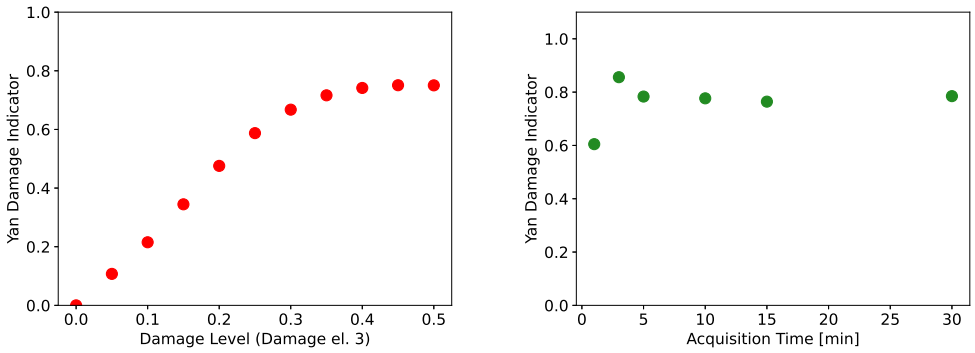

Figure 8: On the left: Sensitivity analysis on damage level percentage. On the right: Sensitivity analysis on acquisition time duration.

7, and these latter reached Yan DI maximum absolute values around time shift equal to 88. Indeed, the results of this initial sensitivity analysis suggested adopting in this case an active space dimension equal to two which is consistent with the higher non-zero singular values, and, in order to mitigate the computational effort, employing a time shift equal to 23.

Thereafter the above-mentioned parameters have been identified, another subsequent sensitivity analysis has been conducted in order to show the influence of the damage level percentage on the Yan et al. DI value for a certain identical input vibration and for the undamaged and damaged case illustrated in the previous sections. The damage level in element 3 of the finite element model (FEM) depicted in Figure 3 has been analyzed in a discrete way from 5% to 50% of cross-section reduction with 5% constant step size. Basically, in real-world scenarios with conventional standard environmental exposure conditions, severe damages have been reported reaching up to 30% of cross section losses at the end of the structure's nominal life [64, 65]. Nonetheless, with specific environmental exposure conditions, chloride attacks, pitting corrosion, and crevice corrosion may lead to dramatic cross section losses of up to 50% [66, 67]. Therefore, in the current preliminary study, the authors analyzed cross section losses up to 50%, still representing a sort of reasonable boundary thus reflecting real-world advanced corrosion scenarios. As illustrated in Figure 8, even for low levels of damage after the undamaged case, Yan et al. DIs assume non-zero values, highlighting the presence of structural performance degradation. The indicators assume a monotonic behavior with progressively increasing values for a higher level

Table 4: Empirical sensitivity analysis of the damage location influence on the Yan et al. damage indicator.

Damaged element	Yan et al. Damage Indicator
1	0.760716
3	0.783350

of damage, showing a virtually constant state around 0.8 when approaching 50% cross-section reduction. Further empirical sensitivity analysis has been conducted regarding the acquisition time duration. In particular, leaving the same random seed for input noise reproducibility purposes, 6 different measurement session duration have been considered: 1 minute, 3 minutes, 5 minutes, 10 minutes, 15 minutes, and 30 minutes. As depicted in Figure 8, acquisition time duration even influences the Yan et al. DI producing quite scatter values for very short acquisition durations. On the other hand, from 5 minutes to 30 minutes, Yan's et al. DIs seem to be no more influenced by the measurement session duration.

Specifically, an acquisition time of 5 minutes duration may virtually be addressed as the best trade-off between computational efficiency effort and damage identification resolution. Another empirical sensitivity analysis has been conducted in order to investigate how the damaged element location can influence the Yan et al. DI. In particular, two extremal cases have been analyzed, i.e. when the damaged element is element 3 in Figure 3 as illustrated in the previous section damage case and when the damaged element is a terminal one (e.g. the element 1). The damage percentage has been considered as 50% of cross-section reduction for both cases. Despite the currently studied slender beam problem is mainly governed by flexural behavior, as described in Table 4, the damage located in element 3 creates very little influence on the Yan et al. DI with respect to the case when only element 1 is damaged with the same percentage entity. This demonstrated that, even if input acceleration is applied only in the left support, the elastic wave celerity makes the perturbation propagation to be quite instantaneous in the FE beam numerical model.

3.4. Dataset collection and ANN multiclass classification problem

Afterward, the empirical sensitivity analysis has been performed, the main parameters governing the numerical problem were set, and, then, time histories numerical simulations were conducted. The numerical test was carried out considering two main situations: the reference undamaged state and

Table 5: Summary of the properties of the implemented MLP. None means variable dimension, depending on the batch chosen size (in this case empirically set to 200). In this case, input units are referred to method (B).

Layer	**Output Shape**	**Activation Function**	**Parameters Number**
Input Layer	[(None, 61)]	-	0
Hidden Layer	(None, 10)	ReLU	620
Output Dense Layer	(None, 3)	Softmax	33

Total Trainable parameters: 653
Epochs: 1000 (also with Early Stopping)
Loss: Categorical Cross-entropy (Optimizer: Adam)

a current, possibly damaged, one. For this latter, the algorithm was able to randomly choose among three possible cases: a further *undamaged* situation which, in combination with the reference one, it would virtually lead to a nil Yan et al. DI value; a *low damage* situation, considering a cross-section reduction percentage of 25%; an *high damage* situation, characterized by a cross-section reduction percentage of 50%.

In order to further increase the generality of the results of the present study, for every run, the algorithm randomly selected how many and which elements are considered damaged with the three above-mentioned possible damaged statuses. Under these conditions, 5000 numerical simulations were executed, collecting 5 minutes long acceleration time history acquisitions for each structural node of the FE model which simulates the presence of a realistic monitoring system placed on that beam.

After collecting these structural responses both for the reference and the possible damaged status, for each acceleration record, the statistical features in in equations (7a)-(7f) were extracted. Since 5 minutes acquisitions have been recorded for each run with a sampling frequency of 500 Hz, the acceleration vector $\boldsymbol{x}$ in equations (7a)-(7f) presents $n_a = 150000$ components. Since the number of accelerometers inside the beam domain is 5 (excluding the extremal support restraint points), as depicted in Figure 3, for each simulation acquisition, 6 statistical features have been extracted from each accelerometer producing, in total, 30 extracted features. Recalling that for each simulation, two cases have been considered (undamaged status and a possible damaged one), altogether, 60 features have been produced from each algorithm run. Method (A) presented in Figure 1, adopts as input these 60 features. Furthermore, these 60 features, in addition to the most informative Yan et al. DI, have been considered as the input to the MLP method (B) of

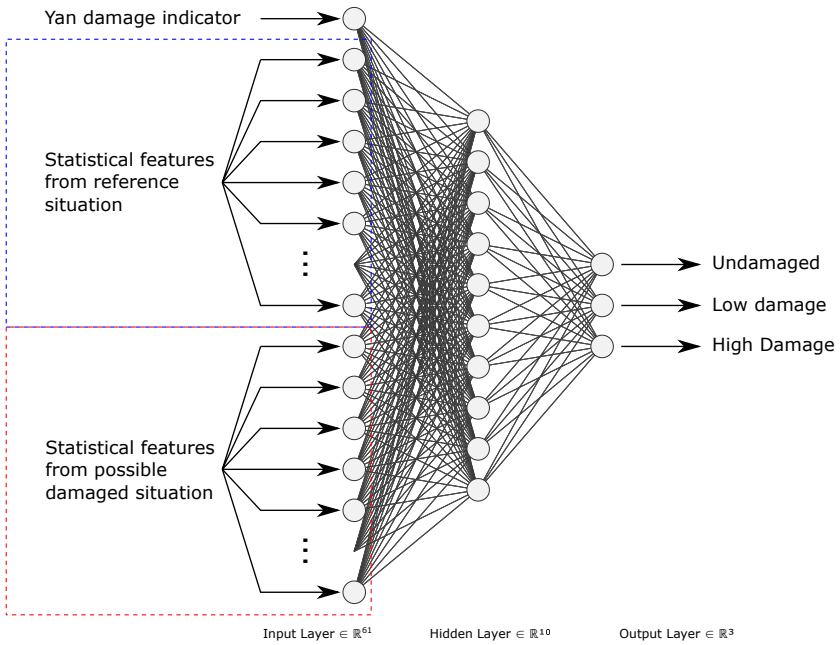

Figure 9: Illustration of the implemented MLP ANN classification model, referring to method (B).

Figure 1, as illustrated in Figure 9. The most informative subspace-based DI was defined through the previous sensitivity analysis by setting a time shift of 23 and an active space dimension of 2. Finally, method (C) of Figure 1 has also been implemented with the same MLP architecture but considering in input many Yan's et al. DIs only. They have been calculated considering all the time shifts from 5 to 25 and truncation orders which define active space dimensions from 1 to 4, collecting in total 80 MLP input features for every one of the 5000 simulations. These values have been identified in the previous sensitivity analysis to be reasonable intervals to detect all the main variations and hidden patterns in the subspace-based DIs, even containing the required computational effort.

The MLP adopted in the current study presents a single hidden layer, with 10 units, which have been empirically found to be the best trade-off between accuracy performances and computational effort avoiding typical machine learning issues such as overfitting and underfitting [68, 69]. The summary of the current MLP properties model is reported in Table 5. It is worth noting that the trainable weights are not usually considered in the

input layer because it only transmits the information to the next layer [68]. The activation function for the hidden layer is the ReLu function in order to avoid negative values reaching the output layer, which instead incorporates a softmax activation function suitable for classification tasks [68, 69].

The multiclass classification MLP adopts the strategy *one-versus-the-rest*, or also acknowledged as *one-versus-all* [69], since after collecting the probability of belonging to one of the three output classes, the one which presents the highest score is denoted as the selected class [70]. The loss adopted in the current problem is the categorical cross-entropy which has been solved by the Adam optimizer algorithm [68, 69, 71, 72].

3.5. MLP multiclass classification results

The (A), (B) and (C) above-mentioned MLP ANN models have been implemented in order to deal with a multiclass classification problem, with three possible outcomes, considering different datasets as illustrated in Figure 1, collected on numerical simulations performed both on a reference undamaged beam model and a possible damaged one.

The only way to assess the performance of the model is to subdivide the entire dataset into at least two subsets: the training set which is employed to train the model permitting learning the optimal weights to successfully tackle the classification problem, and a test set which allows testing the predictive capabilities of the trained model when unseen data are given as inputs (generalization error) [70]. A further partition inside the training set determines the so-called validation set which allows evaluating accuracy performance "online", i.e. during the training phase among the epochs. In the current study, a typical split percentage of 80% of the dataset split has been set for the training set and a 20% has been entrusted to the test set. Instead, the validation set size has been set to 10% of the training set.

For instance, Figure 10 (a) depicts the (A) proposed method MLP performances during the training phase. In particular, the loss function both for the training and the validation sets is depicted over the epochs, reporting also on the same graph the accuracy for both sets. It is worth noting that when the validation loss starts to increase after a monotonic decreasing behavior, at that point the overfitting of the model is reached. In the current plot, the validation loss is still decreasing and only in the very last epochs start to flatten out, without reaching yet the overfitting point and evidencing also a constant overall accuracy from epoch 600 until the end. The performance of

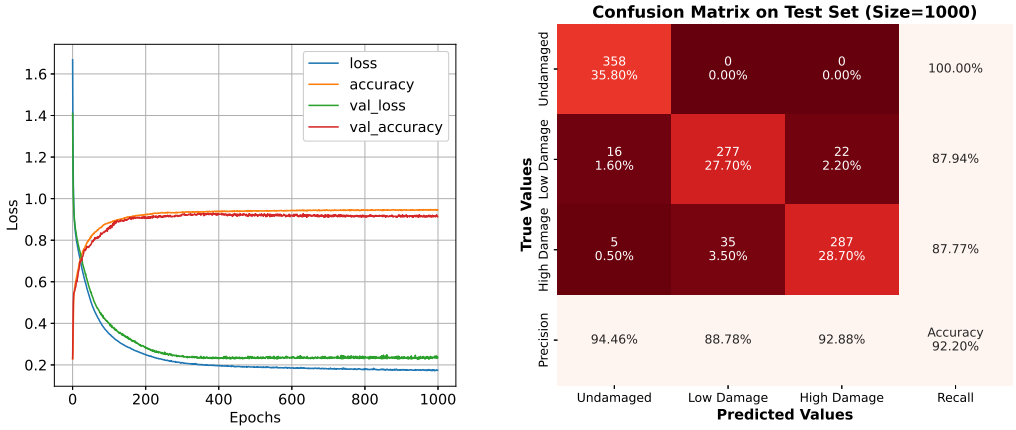

(a) (b)

Figure 10: MLP multiclass classification results for method (A). (a) MLP convergence curves; (b) MLP confusion matrix on the test set.

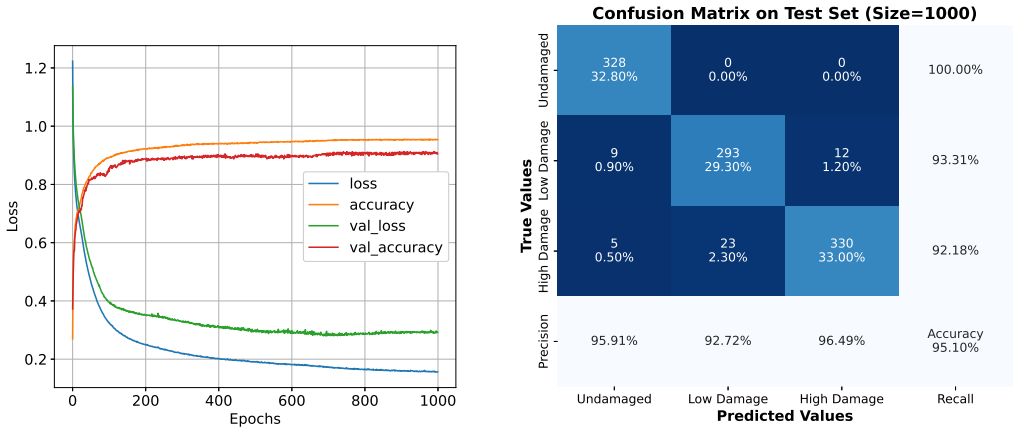

(a) (b)

Figure 11: MLP multiclass classification results for method (B). (a) MLP convergence curves; (b) MLP confusion matrix on the test set.

the trained model (A) has been validated with the test set, whose classification results have been condensed in the confusion matrix illustrated in Figure 10 (b). The overall accuracy obtained is about 92.20% and it measures the portion of the validation set which has been correctly classified (the sum of

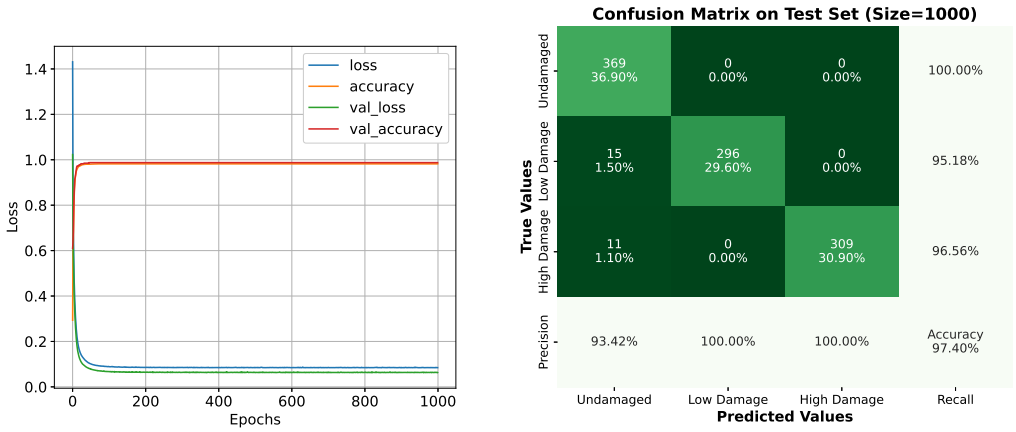

(a) (b)

Figure 12: MLP multiclass classification results for method (C). (a) MLP convergence curves; (b) MLP confusion matrix on the test set.

main diagonal terms) out of the entire validation set size (1000 samples). Two other metrics are presented in the confusion matrix: precision and recall. The precision measures the number of samples correctly classified in a certain class over the total number of samples which have been associated with that class, whereas the recall represents the number of samples correctly classified to a certain class over the number of samples which actually belongs to that class [69]. Therefore, considering the position of the true values along the vertical axis and the predicted values along with the horizontal one, summing the elements of the confusion matrix along the rows for a certain column, it is possible to get the number of samples associated with that column. On the other hand, by summing the elements of the confusion matrix along the column for a certain row, it is possible to get the number of samples that actually belong to that row. In other words, focusing on a certain class (column), the precision evaluates how the predictor performs well, concerning when it associates always that class even if in reality the true class was another one (false positives). Instead, focusing on a certain true class (row), the recall evaluates the predictor performance in terms of correctness of classification with respect to the ground truth, i.e. the actual number of elements which have supposed to belong to that class and even considering the so-called false negative. In this case, both the precision val-

ues and the recall values are quite high, above 87% for all the classification possible outcomes.

Figure 11 (a) depicts the (B) proposed method MLP performances during the training phase, evidencing the absence of overfitting issues. From a deeper insight into the loss and accuracy trends, it would virtually be possible to stop the training to epoch 850, in order to save computational cost and obtain almost the same performances. The performance of the trained model (B) has been validated with the test set, whose classification results have been condensed in the confusion matrix illustrated in Figure 11 (b). The overall accuracy obtained is about 95.10% and it measures the portion of the validation set which has been correctly classified (the sum of main diagonal terms) out of the entire validation set size (1000 samples). As expected, the presence of the most informative Yan's et al. DI with the statistical feature inputs provides better classification performance to the trained model. The higher classification of method (B) with respect to method (A) proves that this most informative subspace-based feature improves the classification performances of the ANN model in Level 1 of the SHM task.

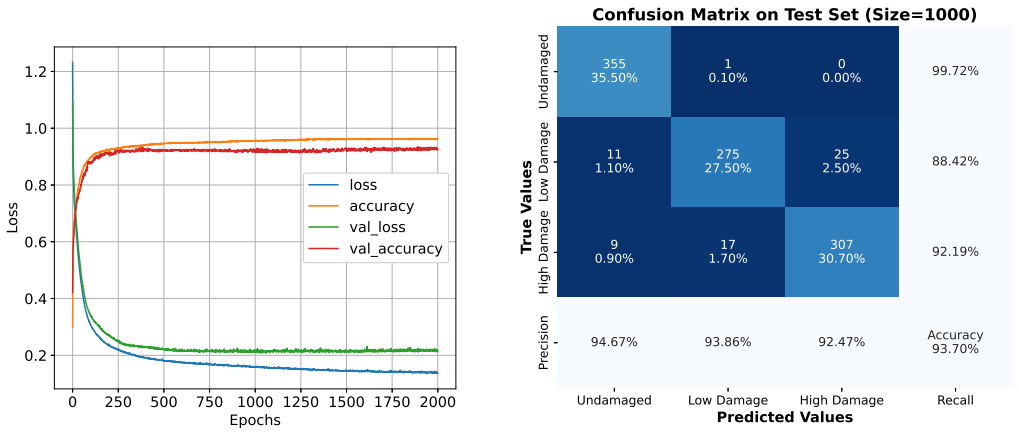

(a) (b)

Figure 13: MLP with dropout regularization multiclass classification results for method (B). (a) MLP convergence curves; (b) MLP confusion matrix on the test set.

Afterward, Figure 12 (a) depicts the (C) proposed method MLP performances during the training phase, evidencing, even in this case, the absence of any overfitting issues. From a deeper insight into the loss and accuracy

trends, it would virtually be possible to stop the training downright to epoch 150, in order to greatly save computational cost and obtain almost the same performances. The performance of the trained model (C) has been validated with the test set, whose classification results have been condensed in the confusion matrix illustrated in Figure 12 (b). The overall accuracy obtained is about 97.40% and it measures the portion of the validation set which has been correctly classified (the sum of main diagonal terms) out of the entire validation set size (1000 samples). As expected, the presence of Yan's et al. DIs only provides better classification performance to the trained model with respect to the previous cases. The outstanding higher classification performance of method (C) with respect to methods (A) and (B) proves that considering an entire set of informative subspace-based features remarkably improves the classification performances of the ANN model for the damage detection task. Furthermore, the advantage of method (C) is that removes the arbitrary choice of the user about governing parameters in the subspace-based DI calculations.

Some further regularization techniques have also been adopted in method (B) of Figure 1, attempting to improve the model accuracy and reduce the computational effort. The early stopping criterion may even be regarded as a form of regularization because it stops the algorithm when the error on a part of the training set begins to rise. Thus, it may actually restrict the parameter search space [68]. A dropout regularization has been even applied to the hidden layer in an attempt to improve the performance of the MLP, with a dropout probability of each unit of 40% [70]. However, as shown in Figure 13 (a), it required a greater computational effort and a longer training phase (2000 epoch) to reach barely 93.70% of overall accuracy, as reported in the confusion matrix depicted in Figure 13 (b). Focusing on the history diagram, it is possible to see that the main effect of the dropout regularization is slowing the learning rate, but this reflects a more regular training behavior considering both the loss and the accuracy trends compared with Figure 11. Furthermore, the random dropout of some units provides a more resilient ANN model, in which the weights are learned to work even when some neurons are completely ignored [70].

Finally, another variant of method (B) has been implemented, denoted as (B)-worsened. In this case, the (B)-worsened method adopts as input the statistical features joined with a bad choice of subspace-based DI governing parameters, which leads to a poorly informative Yan's et al. indicator. In particular, considering all previously calculated DIs for method (C), it has

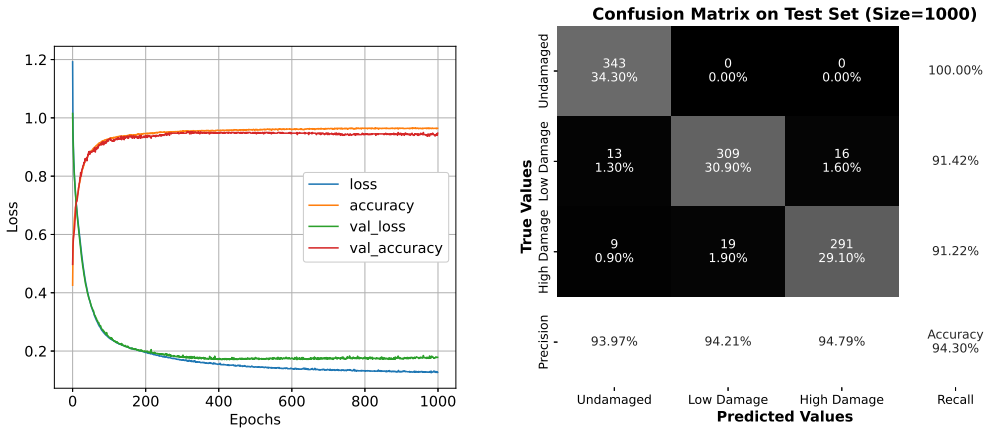

(a) (b)

Figure 14: MLP multiclass classification results for method (B)-worsened. (a) MLP convergence curves; (b) MLP confusion matrix on the test set.

been empirically identified that a bad choice could be virtually associated with a time shift equal to 10 for an active space of dimension 1 for all of the 5000 simulations. Figure 14 (a) depicts the variant (B)-worsened method MLP performances during the training phase, evidencing also here the absence of overfitting issues. From a deeper insight into the loss and accuracy trends, it would be virtually possible to stop the training to epoch 400, in order to save computational cost and obtain almost the same performances. The performance of the trained model (B)-worsened have been validated with the test set, whose classification results have been condensed in the confusion matrix illustrated in Figure 14 (b). The overall accuracy obtained is about 94.30% and it measures the portion of the validation set which has been correctly classified (the sum of main diagonal terms) out of the entire validation set size (1000 samples). As demonstrated in this last example, even with a poor choice of a less informative subspace-based DI, since it is still more sensitive to structural damage, this always improves the classification accuracy performances with respect to method (A), which relies on statistical features only. This demonstrates the robustness of the proposed method because, even considering a less informative but still more sensitive DI, this further improves the model capacities to effectively fulfill the Level 1 of SHM.

In conclusion, the current MLP is able to provide quite interesting multi-class classification results considering the statistical time series features coupled with Yan's et al. subspace DI, extending the capabilities of the MLP model trained in [38]. Furthermore, a good generalization of the current deep learning model is related to the fact that the 5000 numerical simulations randomly considered both how many damaged elements to take into account (even none) and the level of damage to associate with those selected elements. This produced time-series signals which cover many different cases, which were anyway successfully traced back to three possible classification results: undamaged situation, low damage status (cross-section reduction of about 25%), and high damage condition (cross-section reduction of about 50%).

4. Experimental test on a steel I-beam

The authors arranged a real-world monitoring setup in order to experimentally validate the three methods (A), (B), and (C) proposed in the current document. The experimental setup is composed of a simply supported steel I-beam with a span length of $L = 3.540$ m. The cross section is characterized by a depth equal to 80mm and a base width of 40mm, with a flange width of 5mm and a web width of 4mm. As illustrated in Figure 15, four uni-axial velocimeter sensors have been adopted in the current case, placed every 0.708 m on the beam length, in order to collect the vertical vibration response of the beam. The acquisition system of the measured signals was composed of an oscilloscope with 200 MHz of bandwidth (-3 dB) at 50 Ω input impedance and 4 analog channels. The velocimeter sensors consist of a spring-suspended wire coil moving inside a magnetic field, thus capturing voltage deviations with respect to their baseline response. This latter is defined by the sensor's natural frequency, in this case, equal to $10 \pm 3.5\%$ Hz. This kind of sensor represents the ideal cost-effective and high-sensitivity solution for SHM able to capture the natural frequency of structures above the sensor natural frequency [15, 73]. Thus, before adopting the proposed MLP-based damage detection methodologies, the authors conducted the OMA analysis on the signals acquired with 1000 Hz of sampling frequency from the steel I-beam for undamaged conditions, to verify that the first vertical mode of the experimental beam was greater than 10 Hz. Since the natural environmental vibration excitation alone was not enough to identify any modal parameter, the authors caused environmental excitation able to activate at least the

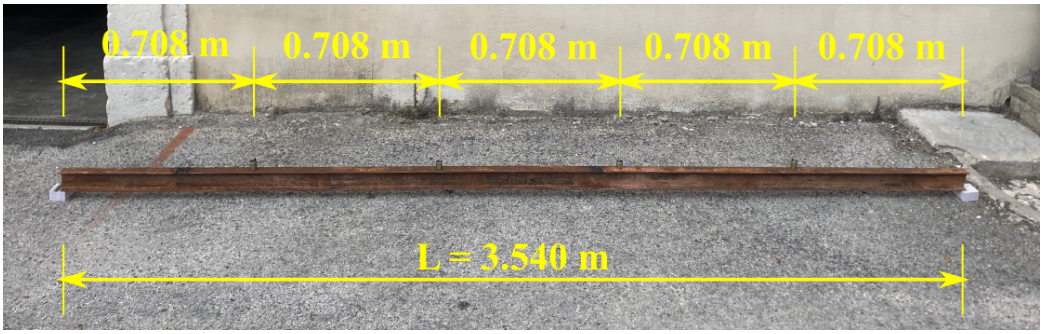

(a)

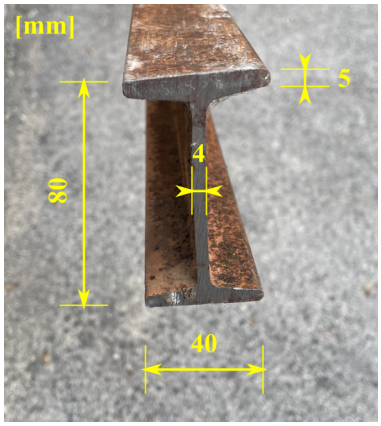

(b)

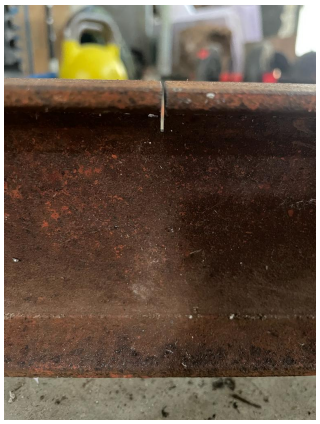

(c)

(d)

Figure 15: Experimental steel beam beam case study. (a) Beam monitoring setup with measures; (b) Beam cross section dimensions; (c) Damage induced with a localized cross section reduction. (d) Velocimeter sensors.

first four vertical modes of the beam by indirectly exciting the surrounding ground with a rubber-headed hammer. Figure 16 (a) demonstrated that the rubber-headed permitted to avoid spikes in the acquired vibration signals, and avoided excessive deviations from the output-only OMA base hypotheses. Figure 16 (b) illustrates the relative stabilization diagram, computed with time shift equal to 15, in which apparently five alignments of stable poles are evidenced. All the pole alignments at 16.92 Hz, 74.27 Hz, 139.05 Hz, and 248.05 Hz appear stables from lower orders up to higher orders, whereas the alignment around 43 Hz appears noisier along the orders. To validate the OMA results, a FEM modal analysis has been conducted. With a preliminary FEM modal analysis, the authors were able to exclude the

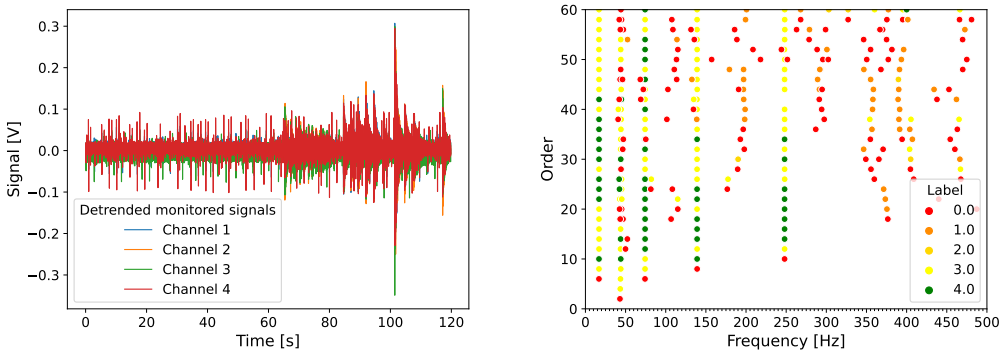

(a) (b)

Figure 16: OMA analysis for undamaged conditions of the experimental beam. (a) Monitored signals expressed in Volt [V]; (b) Resulting stabilization diagram.

alignment around 43 Hz, since it does not represent an actual vertical mode of the structural system. However, the existing steel beam needs a calibration of the flexural rigidity parameter EI, which can be conducted by solving an unconstrained optimization problem leveraging the OMA results according to [74]:

$$\min\ F(EI) = \sum_{i=1}^{n} \left(\frac{f_i^{\text{exp}} - f_i^{\text{calc}}(EI)}{f_i^{\text{exp}}} \right)^2 \tag{9}$$

where $F(EI)$ represents the objective function of the flexural rigidity parameter EI to be minimized, n is the number of considered modes, f_i^{exp} are the experimental frequency obtained from the OMA and the $f_i^{\text{calc}}(EI)$ are obtained as follows, based on the dynamics analytical formulation of a continuous simply supported beam [75, 76]:

$$f_i^{\text{calc}}(EI) = \frac{n^2 \pi}{2L^2} \sqrt{\frac{EI}{\rho A}} \tag{10}$$

in which ρ is the material density equal to 7850 kg/m^3 for structural steel, and A is the cross-section area of the steel I-beam, whose dimensions are reported in Figure 15 (b). Finally, the FEM mode shapes retrieved from OpenSeesPy modal analysis have been reported in Figure 17, evidencing a good agreement with the experimental ones.

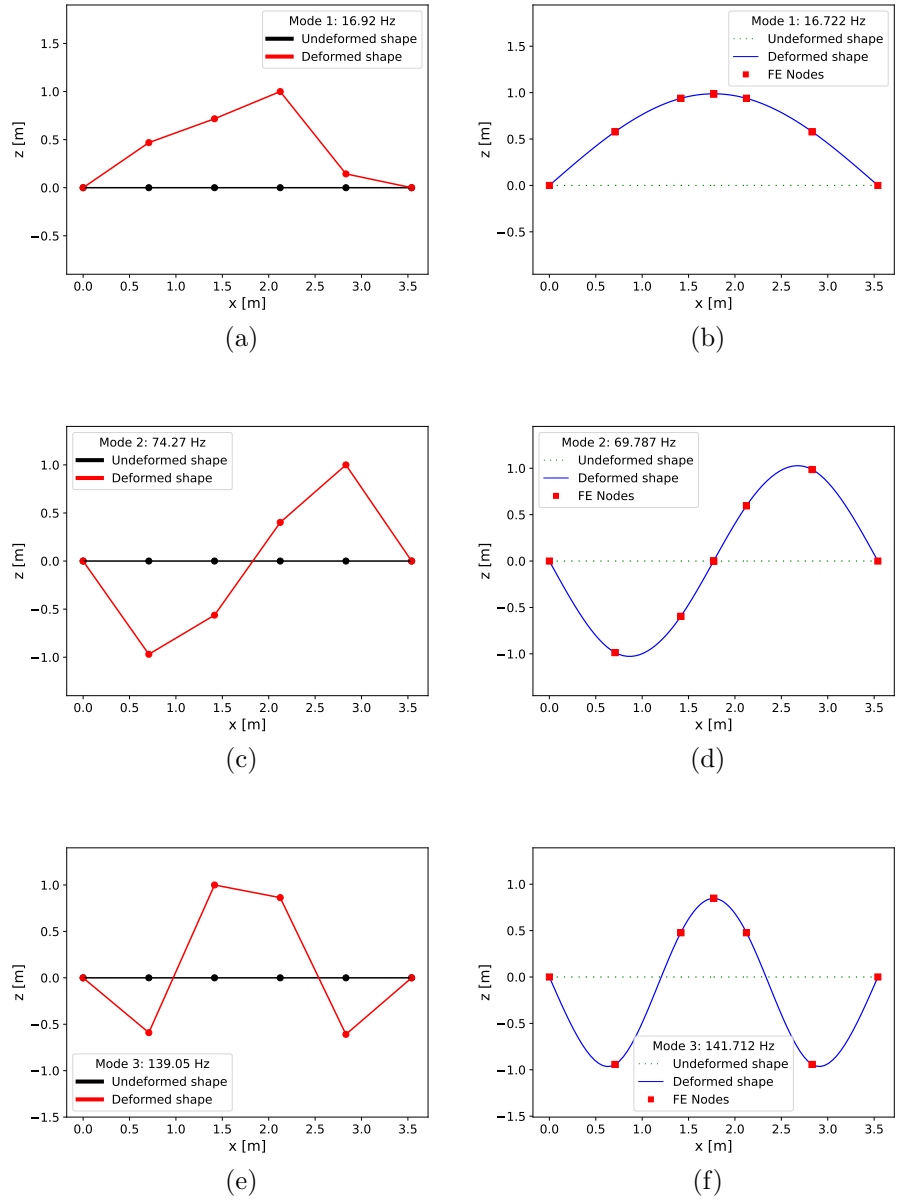

Figure 17: Visualization of the first three mode shapes retrieved from OMA analysis (a)-(c)-(e) and FEM OpenSeesPy modal analysis (b)-(d)-(f), for undamaged conditions of the experimental beam.

Table 6: Summary of the properties of the implemented MLP for the experimental case study. None means variable dimension, depending on the batch chosen size (in this case empirically set to 200). In this case, input units are referred to method (A).

Layer	**Output Shape**	**Activation Function**	**Parameters Number**
Input Layer	[(None, 48)]	-	0
Hidden Layer	(None, 10)	ReLU	490
Output Dense Layer	(None, 2)	Softmax	22

Total Trainable parameters: 512
Epochs: 300
Loss: Categorical Cross-entropy (Optimizer: Adam)

Similarly to the previously discussed numerical study, even in this experimental case, a numerical FEM model was prepared in OpenSeesPy with the OMA-calibrated flexural rigidity in order to simulate five-minutes time-histories vibration responses database under various white noise Gaussian excitation with PGA of 0.01 g and with different damage scenarios. To collect the vibration response of the simulated I-beam, the nodes of the model have been placed accordingly to the actual sensors' placement along the beam, see Figure 15 (a). As depicted in Figure 15 (c), in this realistic scenario, the damage has been introduced as punctual damage, by locally reducing the cross-section. Therefore, in total 5000 FEM simulations have been conducted both in a reference (undamaged) state and in a current (possibly damaged) state, with different punctual damages randomly located along the beam and with a possible entity of 0%, 5%, 10%, 15%, or 20% of cross section reduction. With a deeper insight into these 5000 FEM simulations, it was possible to notice an unbalanced number of undamaged scenarios, randomly occurring only in 965 simulations. Despite the unbalance between the two healthy and damaged classes may produce biased training toward the damage scenario with respect to the undamaged one, the authors leveraged this fact to show if the damage-sensitive features are effective and discriminative enough to ensure a good training of the MLP models even with a biased dataset, a condition which usually occurs in real-world situations.

In order to show a realistic application of the three proposed intelligent damage detection methods, the authors trained the neural models with only two output classes, i.e. healthy or damaged, acting therefore as an anomaly detection procedure. The numerical FEM model of the experimental beam permitted training the neural models, which have been finally tested on real vibration acquisitions from the experimental setup thereafter. The MLP has

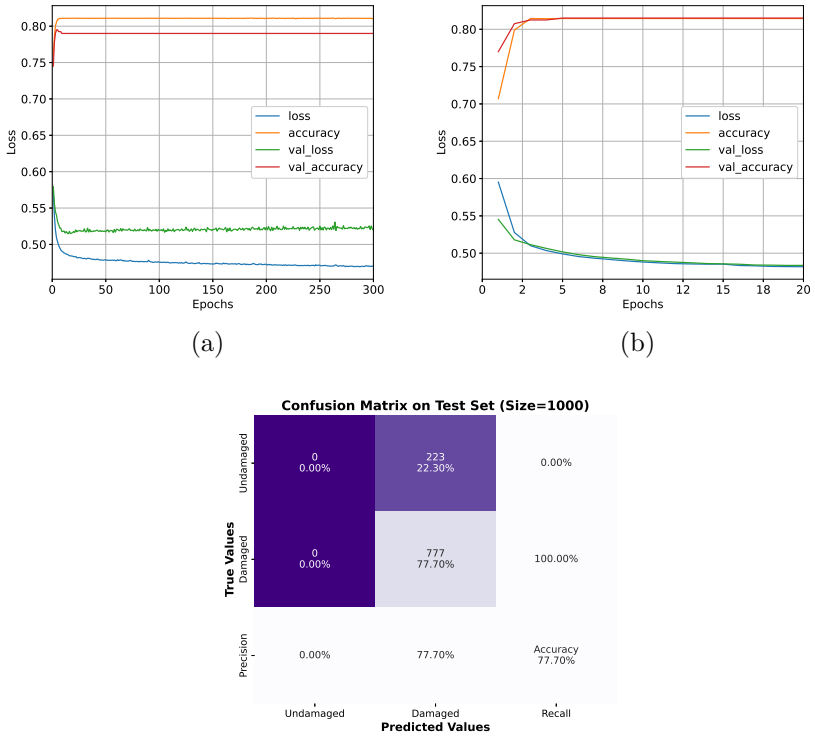

Figure 18: MLP training performances for method (A) on simulated I-beam. (a) 300 epochs with evidence of overfitting; (b) 20 epochs due to early stopping; (c) Confusion matrix on the test set.

been chosen with a hidden layer with 10 units as reported in Table 6. As before, to effectively train the MLP models, datasets of damage-sensitive features have been collected from the 5000 simulated time history responses for each of the three proposed methods (A), (B), and (C). Afterward, every dataset of features has been subdivided into two parts: the 80% composed the training set, whereas the remaining 20% is the test set. The validation set size has been set equal to 10% of the training set.

Method (A) presented in Figure 1 is based on the calculation of six features eq.(7a)-(7f) from the time history responses of each sensor. Thus, considering four velocimeter sensors and two states, i.e. the reference and the current one, the input feature vector to the MLP for method (A) has a

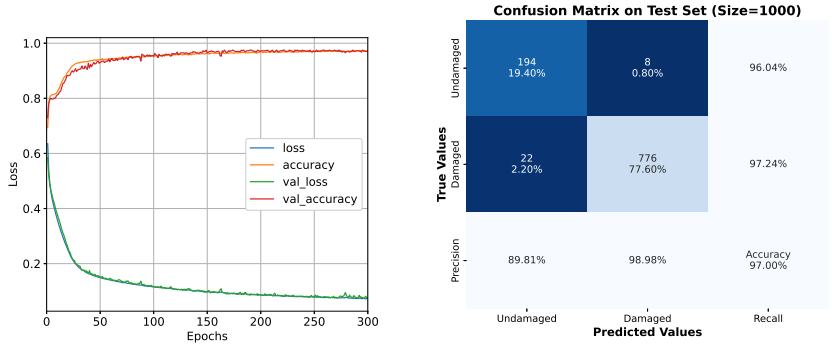

(a) (b)

Figure 19: MLP training performances for method (B) on simulated I-beam. (a) 300 epochs withou any evidence of overfitting; (c) Confusion matrix on the test set.

dimension of 48. The results of the training of the MLP for method (A) are reported in Figure 18. As demonstrated in Figure 18 (a), the convergence curves over 300 epochs highlighted overfitting issues occurring from around epoch number 20 due to the increasing trend of validation loss. Therefore, the early stopping procedure was employed by limiting the training over 20 epochs, as reported in Figure 18 (b). Nevertheless, with punctual damage, statistical features of the time series responses were not sufficiently discriminative between damaged and undamaged cases. Indeed, as depicted in Figure 18 (c), the confusion matrix on the test set revealed a biased behavior of the MLP for method (A) toward the damaged class, reflecting the biased unbalance of the 5000 simulations.

On the other hand, method (B) presented in Figure 1 relies on the calculation of the same six features of method (A) eq.(7a)-(7f) for every sensor and additionally considering also a subspace-based Yan's et al. damage sensitive feature [45]. In accordance with the numerical case study analyzed in previous sections, for the subspace-based Yan's et al. DI calculation it was set a time shift of 23 and an active space dimension of 2. Thus, the input feature vector to the MLP for method (B) has a dimension of 49. The results of the training of the MLP for method (A) are reported in Figure 19. As demonstrated in Figure 19 (a), the convergence curves over 300 epochs evidenced that no overfitting issues occurred because of a monotonic decreasing trend of the validation loss. Therefore, the confusion matrix on the test set for method (B) reported in Figure 19 (b) demonstrated the benefits of

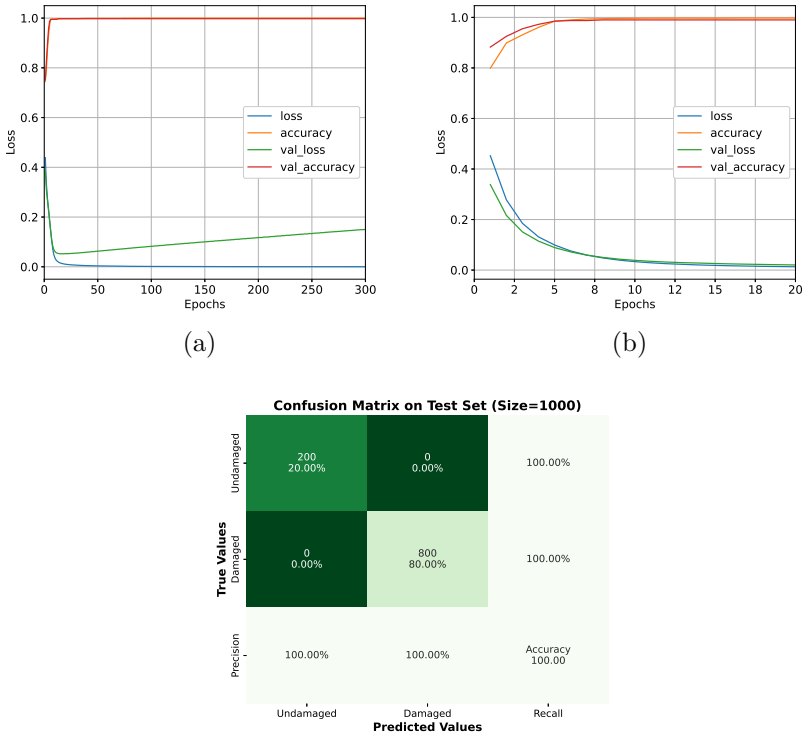

Figure 20: MLP training performances for method (C) on simulated I-beam. (a) 300 epochs with evidence of overfitting; (b) 20 epochs due to early stopping; (c) Confusion matrix on the test set.

considering a subspace-based DI in addition to the statistical features. Actually, the additional information carried with Yan's et al. DI substantially improved the training performance of method (A), and now the trained MLP for method (B) does not reflect anymore the biased unbalance of the 5000 simulations. The Yan's et al. subspace indicator thus provided more discriminative features which substantially helped the MLP model to correctly classify damaged and undamaged samples.

Eventually, method (C) presented in Figure 1 relies on the calculation of an entire dataset composed of subspace-based Yan's et al. damage sensitive feature only, as explained in 3.4. In accordance with the numerical case study analyzed in previous sections, these DIs have been calculated consider-

ing all the time shifts from 5 to 25 and truncation orders which define active space dimensions from 1 to 4. Thus, the input feature vector to the MLP for method (C) has a dimension of 80. The results of the training of the MLP for method (C) are reported in Figure 20. As demonstrated in Figure 20 (a), the convergence curves over 300 epochs highlighted overfitting issues occurring from around epoch number 20 due to the increasing trend of validation loss. Therefore, the early stopping procedure was employed by limiting the training over 20 epochs, as reported in Figure 20 (b). Since the benefits of Yan's et al DIs have been already demonstrated before, even with small and punctual damages their informative content is very effective and discriminative between damaged and undamaged cases. Figure 20 (c) illustrates that the confusion matrix on the test set revealed the outstanding behavior of the MLP for method (C) by correctly classifying all the samples of the so far unseen simulated test set.

In conclusion, the authors tested the numerically trained MLP for the three methods (A), (B), and (C) with vibration responses collected from the experimental setup in five different scenarios, denoted as 1 to 5. The first scenario is referred to as the undamaged situation and was identified as the reference situation, whereas all the scenarios from 1 to 5 taken individually have been considered alternately as the current state. The scenarios from 2 to 5 represent the steel I-beam with induced punctual damage introduced in the midspan, as depicted in Figure 15 (c). Specifically, the scenarios from 2 to 5 represent progressively increasing damage level situations with a local cross-section reduction of about 5.9%, 11.8% 23.5% 25.7% respectively. In each of the 5 experimental scenarios, the authors collected a few minutes of vibration responses from the four velocimeter sensors placed on the steel I-beam and calculated the input features vector to feed the after-training MLP neural models for the three proposed methods. The prediction results of the trained MLP models have been reported in terms of the confusion matrix in Figure 21. As shown in Figure 21 (a), the poor training performances on numerical simulations of method (A) reflected also on the experimental measurements, whereas methods (B) and (C), Figures 21 (b) and (c) respectively, provided outstanding results correctly classifying the four damage scenarios and the remaining undamaged one.

5. Discussion

In this section, the discussion of the main results obtained for the numer-

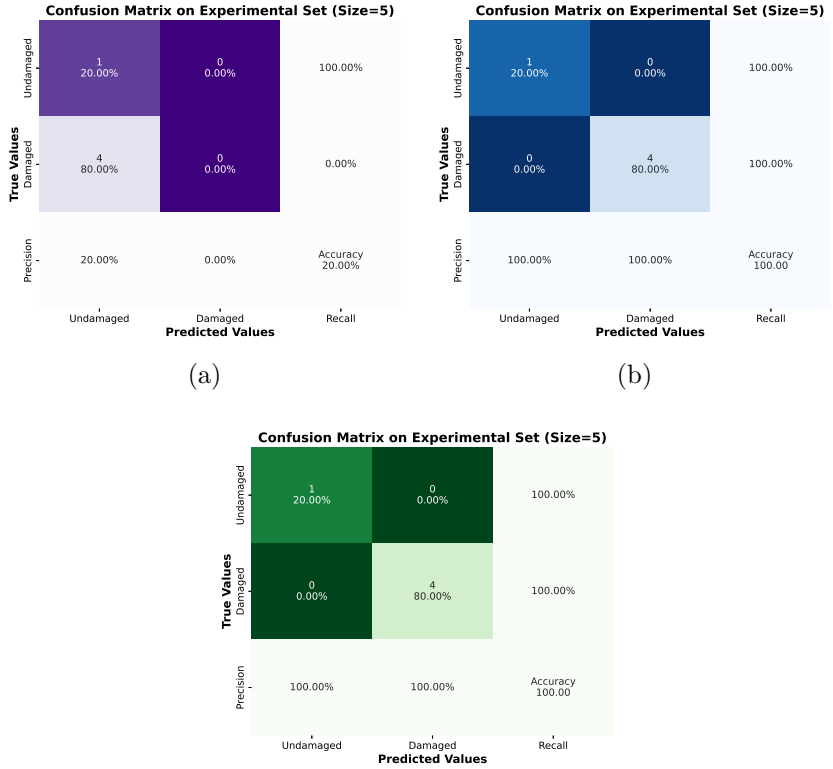

Figure 21: After training MLP predictions on experimental measurements collected from the steel-I beam for one undamaged and four damaged scenarios. (a) predictions of MLP trained with method (A); (b) predictions of MLP trained with method (B); (c) Predictions of MLP trained with method (C).

ical and experimental setups is presented.

Figure 22 illustrates a bar graph comparing the overall accuracy levels of the proposed methods for the numerical case study of section 3.4. Method (A), leads to a quite good accuracy level of almost about 92% with statistical features only, but the accuracy classification performances absolutely increased to 95% when, in method (B), the most informative subspace-based DI has been added to the inputs, see section 3.3. Even considering a poorly informative subspace-based DI, as in method (B)-worsened, the performances have still boosted to 94% with respect to method (A). Furthermore, these results have demonstrated the robustness of the proposed method to couple

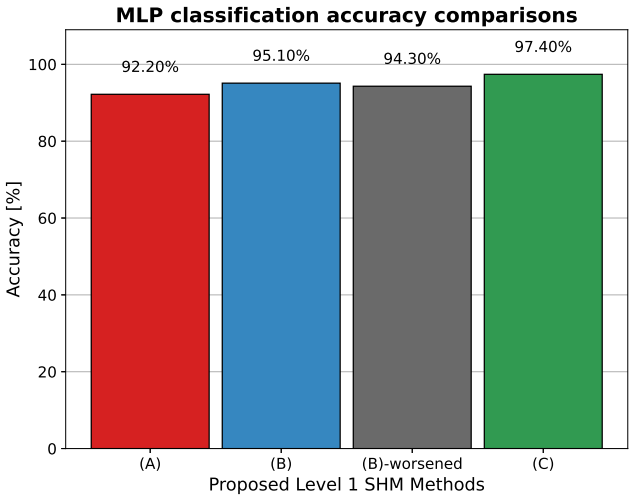

Figure 22: MLP multiclass classification comparisons in terms of accuracy metric among the proposed methods (A), (B), (B)-worsened, (C).

Yan's et. al. indicators with the statistical features. Indeed, the association of statistical features with a more damage-sensitive indicator has produced better results than considering statistical features alone. Finally, outstanding accuracy performance results have been obtained with method (C), which reaches about 97%. The main advantage of method (C) is related to the fact that it considers as an input dataset many subspace-based DIs only, actually removing the user's arbitrary choice of the parameters which affect the DI calculations. Moreover, the MLP is able to take into account more damage-sensitive features only and even consider all the variability and hidden pattern already pointed out e.g. in Figure 7. Finally, further comparisons have been performed in terms of recall and precision as illustrated in Figures 23 and 24. Focusing on the recall metric, for every of the considered methods the undamaged case has been always correctly classified with respect to the belonging class number ground truth (about 100%). These results have proven that MLPs were to learn that the subspace-based DI value tends to be close to zero when an undamaged situation occurred. On the other hand, method (A) reaches the lowest recall both in low damage and high damage classes, whereas the other methods reach values always greater than 91%. These results highlighted the advantages of also considering the subspace-based DI information instead of statistical features only. Rather, focusing on

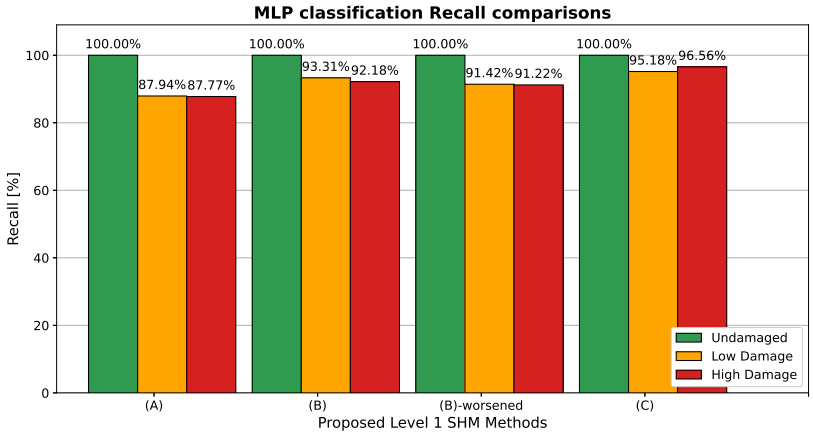

Figure 23: MLP multiclass classification comparisons in terms of recall metric among the proposed methods (A), (B), (B)-worsened, (C).

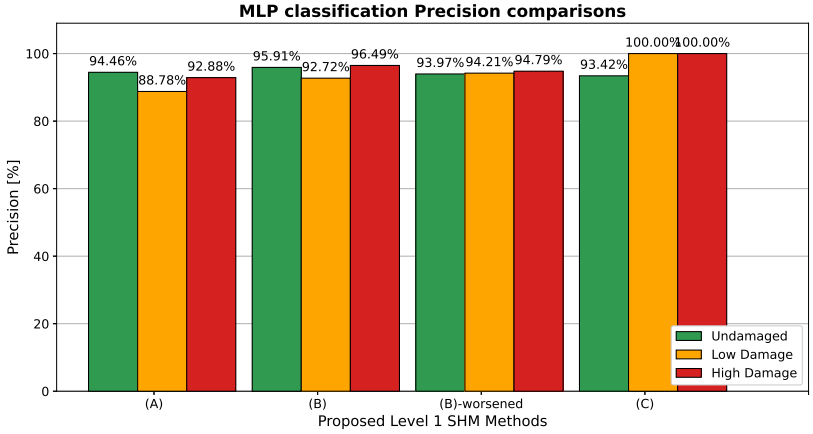

Figure 24: MLP multiclass classification comparisons in terms of precision metric among the proposed methods (A), (B), (B)-worsened, (C).

precision metric, method (B) presents greater values with respect to (A) and (B)-worsened for all the three classes. Moreover, it is clear from the graph that remarkable precision values have been obtained in method (C) for which 100% have been reached for low damage and high damage. This fact evidences how the MLP has not misclassified the inputs which truly belong to these two latter classes.

Focusing on the experimental test described in section 4, the OMA results

show the effects of uncertainties when dealing with existing structural elements and real measurements, which need a calibration of flexural rigidity to arrange a numerical model which reflects the actual vibrational characteristics of the real structure. The proposed damage classification methodologies have been employed as anomaly detection procedures, with two-class classification, i.e. healthy or damaged classes, in order to illustrate the capabilities of the proposed methodologies for real-world structures. The MLP for the three methods (A), (B), and (C) have been trained on numerically simulated vibrational responses, see Figures 18,19 and 20. Afterward, the three MLP models were tested on the test set of simulated responses, evidencing the effectiveness of the subspace-based DI which provides outstanding results both for methods (B) and (C). Method (A) trained only on statistical features appeared biased toward damage class, evidencing poor informative content of time-series statistical indicators because of the punctual damage situation modeled in this case. Finally, the three trained MLPs were tested on a set of five vibrational responses collected from the real steel I-beam structure, four with damaged and one with undamaged conditions, see Figure 21. The MLP predictions were all correct concerning the ground truth labels for methods (B) and (C) which leverage information from subspace-based DIs. On the contrary, for method (A), conversely to envisaged bias toward the damage situation, MLP classified all five samples as healthy. A possible explanation for the biased classification of real samples toward the healthy state may be related to the fact that real time-series data are characterized by different statistical indicators' numerical values (probably smaller) than the ones that predominate in the simulated responses.

In conclusion, the main relevant results obtained from the current study can be summarized as follows:

- Method (A) which only considers statistical features performed worse than other methods which included subspace-based DIs as input of ANN;
- Method (B)-worsened performed quite similar to method (B), consistently exploiting information contained in the subspace-based DI and statistical features. This result proves the robustness of the proposed method concerning misleading user parameters choice;
- Method (C) exhibited the best performance concerning the other analyzed methods. This method has the advantage of removing the user's

arbitrary choice of the parameters which affect the DIs calculations.

- The effectiveness of methods (B) and (C) have been proven on an experimental test, demonstrating the discriminative and informative content of subspace-based DIs to distinguish among various damaged states.

6. Conclusions and future remarks

Three methods have been proposed to accomplish the damage detection task, i.e. level 1 of the structural health monitoring paradigm. They are based on multi-layer perceptron ANN performing multiclass health states classification on features calculated from output-only vibration data. Method (A) is based on statistical features only calculated on raw time series data, whereas method (B) attempts to enhance method (A) by considering an additional more informative subspace-based damage indicator. However, the calculation of these damage indicators requires the definition of some hyperparameters (time shift and active and null subspace dimensions). Therefore, method (C) relies on an entire set of damage indicators obtained by varying such hyperparameters in a reasonable range, thus avoiding any arbitrary definition of them. A poor arbitrary choice of these hyperparameters may lead to poorly informative damage indicators, thereby method (C) overcomes this issue considering an entire set of possible damage indicator, some more informative, others less so. To test the three methods, a numerical finite element beam model simulated a monitoring system with sensors placed in the correspondence of the finite element nodes, and the test set performances exhibit an overall accuracy higher than 90%. For the sake of further validation purposes, the three methodologies have been finally tested on an experimental steel I-beam setup, evidencing the effectiveness of informative subspace-based damage indicators in methods (B) and (C).

In summary, this study demonstrated that the proposed methodologies may be implemented as a damage anomaly detection and warning system comparing a reference state, i.e. when the monitoring starts, and a current state, i.e. any subsequent moment. In this sense, the artificial-neural-network-based model act as anomaly detection for new vibration response data by recalling the predictions of the after-training model, which is quite fast in usage. However, the main drawback of the proposed methods is related to the requirement of a great amount of finite element simulations, i.e. with a considerable computational effort, to forecast possible damages which may

occur in the structure and effectively train the ANN-based models. Furthermore, the experimental test demonstrated that to deal with real structures, accurate FE models are required which effectively capture the dynamical behavior of the existing structure, i.e. thus calibrating flexural rigidity based on operational modal analysis results. Future developments will explore the extension of the proposed methodologies to the other levels of the structural health monitoring paradigm. Furthermore, it would be of significance to analyze the effects on the subspace-based damage indicators and the proposed methodology considering more realistic load case conditions, e.g. analyzing moving load simulating traffic in-service conditions.

References

[1] M. Döhler, F. Hille, L. Mevel, W. Rücker, Structural health monitoring with statistical methods during progressive damage test of s101 bridge, Engineering Structures 69 (2014) 183–193. doi:https://doi.org/10.1016/j.engstruct.2014.03.010.

[2] G. C. Marano, G. Quaranta, A new possibilistic reliability index definition, Acta mechanica 210 (3) (2010) 291–303.

[3] M. Z. Sarwar, D. Cantero, Deep autoencoder architecture for bridge damage assessment using responses from several vehicles, Engineering Structures 246 (2021) 113064. doi:https://doi.org/10.1016/j.engstruct.2021.113064.

[4] H. Salehi, R. Burgueño, S. Chakrabartty, N. Lajnef, A. H. Alavi, A comprehensive review of self-powered sensors in civil infrastructure: State-of-the-art and future research trends, Engineering Structures 234 (2021) 111963. doi:https://doi.org/10.1016/j.engstruct.2021.111963.

[5] D. Feng, M. Q. Feng, Computer vision for shm of civil infrastructure: From dynamic response measurement to damage detection – a review, Engineering Structures 156 (2018) 105–117. doi:https://doi.org/10.1016/j.engstruct.2017.11.018.

[6] A. Aloisio, M. M. Rosso, R. Alaggio, Experimental and analytical investigation into the effect of ballasted track on the dynamic response of railway bridges under moving loads, Journal of Bridge Engineering 27 (10) (2022) 04022085.

[7] S. J. Idehara, M. Dias Junior, Modal analysis of structures under non-stationary excitation, Engineering Structures 99 (2015) 56–62. doi:https://doi.org/10.1016/j.engstruct.2015.04.035.

[8] P. Singh, M. Keyvanlou, A. Sadhu, An improved time-varying empirical mode decomposition for structural condition assessment using limited sensors, Engineering Structures 232 (2021) 111882. doi:https://doi.org/10.1016/j.engstruct.2021.111882.

[9] C. Ye, L. Butler, F. Huseynov, C. Middleton, Evaluating in-service structural behaviour of an operational railway bridge using fibre optic sensing and structural model updating, Engineering Structures 247 (2021) 113116. doi:https://doi.org/10.1016/j.engstruct.2021.113116.

[10] A. D. Orcesi, D. M. Frangopol, A stakeholder probability-based optimization approach for cost-effective bridge management under financial constraints, Engineering Structures 33 (5) (2011) 1439–1449. doi:https://doi.org/10.1016/j.engstruct.2010.12.035.

[11] E. N. Tochaei, Z. Fang, T. Taylor, S. Babanajad, F. Ansari, Structural monitoring and remaining fatigue life estimation of typical welded crack details in the manhattan bridge, Engineering Structures 231 (2021) 111760. doi:https://doi.org/10.1016/j.engstruct.2020.111760.

[12] M. M. Rosso, G. Marasco, S. Aiello, A. Aloisio, B. Chiaia, G. C. Marano, Convolutional networks and transformers for intelligent road tunnel investigations, Computers & Structures 275 (2023) 106918.

[13] A. Fiore, G. Quaranta, G. C. Marano, G. Monti, Evolutionary polynomial regression–based statistical determination of the shear capacity equation for reinforced concrete beams without stirrups, Journal of Computing in Civil Engineering 30 (1) (2016) 04014111.

[14] G. Marano, G. Quaranta, G. Monti, Modified genetic algorithm for the dynamic identification of structural systems using incomplete measurements, Computer-Aided Civil and Infrastructure Engineering 26 (2) (2011) 92–110. doi:10.1111/j.1467-8667.2010.00659.x.

[15] R. Brincker, C. E. Ventura, Introduction to Operational Modal Analysis, John Wiley & Sons, Ltd, 2015. doi:https://doi.org/10.1002/9781118535141.

[16] A. Poulimenos, S. Fassois, Parametric time-domain methods for non-stationary random vibration modelling and analysis — a critical survey and comparison, Mechanical Systems and Signal Processing 20 (4) (2006) 763–816. doi:https://doi.org/10.1016/j.ymssp.2005.10.003.

[17] S. Das, P. Saha, S. Patro, Vibration-based damage detection techniques used for health monitoring of structures: a review, Springer Journal of Civil Structural Health Monitoring 6 (2016) 477–507. doi:https://doi.org/10.1007/s13349-016-0168-5.

[18] C. Rainieri, G. Fabbrocino, Operational Modal Analysis of Civil Engineering Structures, Springer Science+Business Media New York 2014, 2014, an Introduction and Guide for Applications. doi:https://doi.org/10.1007/978-1-4939-0767-0.

[19] J. Brownjohn, F. Magalhaes, E. Caetano, A. Cunha, Ambient vibration re-testing and operational modal analysis of the humber bridge, Engineering Structures 32 (8) (2010) 2003–2018. doi:https://doi.org/10.1016/j.engstruct.2010.02.034.

[20] R. Sarlo, P. A. Tarazaga, M. E. Kasarda, High resolution operational modal analysis on a five-story smart building under wind and human induced excitation, Engineering Structures 176 (2018) 279–292. doi:https://doi.org/10.1016/j.engstruct.2018.08.060.

[21] M. Gatti, Structural health monitoring of an operational bridge: A case study, Engineering Structures 195 (2019) 200–209. doi:https://doi.org/10.1016/j.engstruct.2019.05.102.

[22] R. Brincker, L. Zhang, P. Andersen, Modal identification of output-only systems using frequency domain decomposition, Smart materials and structures 10 (3) (2001) 441.

[23] B. Peeters, G. De Roeck, Reference-based stochastic subspace identification for output-only modal analysis, Mechanical systems and signal processing 13 (6) (1999) 855–878.

[24] A. Rytter, Vibrational Based Inspection of Civil Engineering Structures, Vol. Fracture & dynamics Vol. R9314 No. 44, Aalborg University, Dept. of Building Technology and Structural Engineering, 1993, ph.D. thesis.

[25] C. Kralovec, M. Schagerl, Review of structural health monitoring methods regarding a multi-sensor approach for damage assessment of metal and composite structures, Sensors 20 (3) (2020). doi:10.3390/s20030826.

[26] Z. Sharif Khodaei, M. Aliabadi, A multi-level decision fusion strategy for condition based maintenance of composite structures, Materials 9 (9) (2016). doi:10.3390/ma9090790.

[27] G. Bernagozzi, C. E. Ventura, S. Allahdadian, Y. Kaya, L. Landi, P. P. Diotallevi, Output-only damage diagnosis for plan-symmetric buildings with asymmetric damage using modal flexibility-based deflections, Engineering Structures 207 (2020) 110015. doi:https://doi.org/10.1016/j.engstruct.2019.110015.

[28] M. P. Limongelli, E. Manoach, S. Quqa, P. F. Giordano, B. Bhowmik, V. Pakrashi, A. Cigada, Vibration Response-Based Damage Detection, Springer International Publishing, Cham, 2021, pp. 133–173.

[29] N. Stubbs, J.-T. Kim, Damage localization in structures without baseline modal parameters, AIAA Journal 34 (8) (1996) 1644–1649. doi:https://doi.org/10.2514/3.13284.

[30] Y.-z. Lin, Z.-h. Nie, H.-w. Ma, Structural damage detection with automatic feature-extraction through deep learning, Computer-Aided Civil and Infrastructure Engineering 32 (12) (2017) 1025–1046. arXiv:https://onlinelibrary.wiley.com/doi/pdf/10.1111/mice.12313, doi:https://doi.org/10.1111/mice.12313.

[31] A. Aloisio, L. Di Battista, R. Alaggio, M. Fragiacomo, Sensitivity analysis of subspace-based damage indicators under changes in ambient excitation covariance, severity and location of damage, Engineering Structures 208 (2020) 110235.

[32] M. Döhler, F. Hille, L. Mevel, Vibration-based monitoring of civil structures with subspace-based damage detection, in: Mechatronics for Cultural Heritage and Civil Engineering, Springer, 2018, pp. 307–326.

[33] H. Shokravi, H. Shokravi, N. Bakhary, S. S. Rahimian Koloor, M. Petrů, Health monitoring of civil infrastructures by subspace system identifi-

cation method: An overview, Applied Sciences 10 (8) (2020). doi:10.3390/app10082786.

[34] A.-M. Yan, P. De Boe, J.-C. Golinval, Structural damage diagnosis by kalman model based on stochastic subspace identification, Structural Health Monitoring 3 (2) (2004) 103–119.

[35] G. Gautier, R. Serra, J.-M. Mencik, Roller bearing monitoring by new subspace-based damage indicator, Hindawi Shock and Vibration 2015 (2008) 11. doi:https://doi.org/10.1155/2015/828093.

[36] E. Balmès, M. Basseville, L. Mevel, H. Nasser, W. Zhou, Statistical model-based damage localization: A combined subspace-based and substructuring approach, Structural Control and Health Monitoring 15 (6) (2008) 857–875. arXiv:https://onlinelibrary.wiley.com/doi/pdf/10.1002/stc.223, doi:https://doi.org/10.1002/stc.223.

[37] K. Saeed, N. Mechbal, G. Coffignal, M. Vergé, Subspace-based damage localization using artificial neural network, in: 18th Mediterranean Conference on Control and Automation, MED'10, 2010, pp. 563–568. doi:10.1109/MED.2010.5547729.

[38] R. P. Finotti, A. A. Cury, F. d. S. Barbosa, An shm approach using machine learning and statistical indicators extracted from raw dynamic measurements, Latin American Journal of Solids and Structures 16 (2) (2019). doi:https://doi.org/10.1590/1679-78254942.

[39] M. M. Rosso, A. Aloisio, R. Cucuzza, D. P. Pasca, G. Cirrincione, G. C. Marano, Structural health monitoring with artificial neural network and subspace-based damage indicators, in: International Conference on Trends on Construction in the Post-Digital Era, Springer, 2023, pp. 524–537.

[40] M. Döhler, L. Mevel, Modular subspace-based system identification from multi-setup measurements, IEEE Transactions on Automatic Control 57 (11) (2012) 2951–2956. doi:10.1109/TAC.2012.2193711.

[41] M. Döhler, L. Mevel, Q. Zhang, Fault detection, isolation and quantification from gaussian residuals with application to structural damage diagnosis, Annual Reviews in Control 42 (2016) 244–256. doi:https://doi.org/10.1016/j.arcontrol.2016.08.002.

[42] S. Allahdadian, M. Döhler, C. Ventura, L. Mevel, Towards robust statistical damage localization via model-based sensitivity clustering, Mechanical Systems and Signal Processing 134 (2019) 106341. doi:https://doi.org/10.1016/j.ymssp.2019.106341.

[43] M. Döhler, L. Mevel, F. Hille, Subspace-based damage detection under changes in the ambient excitation statistics, Mechanical Systems and Signal Processing 45 (1) (2014) 207–224. doi:https://doi.org/10.1016/j.ymssp.2013.10.023.

[44] M. D. H. Bhuyan, E. Viefhues, M. Döhler, Y. Lecieux, L. Mevel, F. Hille, F. Schoefs, Output-only subspace and transfer matrix-based damage localization and quantification, in: IOMAC - 7th International Operational Modal Analysis Conference, Ingolstadt, Germany, 2017.

[45] A.-M. Yan, J.-C. Golinval, Null subspace-based damage detection of structures using vibration measurements, Mechanical Systems and Signal Processing 20 (3) (2006) 611–626. doi:https://doi.org/10.1016/j.ymssp.2005.04.010.

[46] S. Gres, M. D. Ulriksen, M. Döhler, R. J. Johansen, P. Andersen, L. Damkilde, S. A. Nielsen, Statistical methods for damage detection applied to civil structures, Procedia Engineering 199 (2017) 1919–1924, x International Conference on Structural Dynamics, EURODYN 2017. doi:https://doi.org/10.1016/j.proeng.2017.09.280.

[47] E. Parloo, P. GUILLAUME, M. VAN OVERMEIRE, Damage assessment using mode shape sensitivities, Mechanical Systems and Signal Processing 17 (3) (2003) 499–518. doi:https://doi.org/10.1006/mssp.2001.1429.

[48] M. Basseville, M. Abdelghani, A. Benveniste, Subspace-based fault detection algorithms for vibration monitoring, Automatica 36 (1) (2000) 101–109. doi:https://doi.org/10.1016/S0005-1098(99)00093-X.

[49] M. Basseville, L. Mevel, M. Goursat, Statistical model-based damage detection and localization: subspace-based residuals and damage-to-noise sensitivity ratios, Journal of Sound and Vibration 275 (3) (2004) 769–794. doi:https://doi.org/10.1016/j.jsv.2003.07.016.

[50] K. A. Kvåle, O. Øiseth, A. Rønnquist, Operational modal analysis of an end-supported pontoon bridge, Engineering Structures 148 (2017) 410–423. doi:https://doi.org/10.1016/j.engstruct.2017.06.069.

[51] Étienne Balmès, M. Basseville, F. Bourquin, L. Mevel, H. Nasser, F. Treyssède, Merging sensor data from multiple temperature scenarios for vibration monitoring of civil structures, Structural Health Monitoring 7 (2) (2008) 129–142. arXiv:https://doi.org/10.1177/1475921708089823, doi:10.1177/1475921708089823.

[52] C. Fritzen, G. Mengelkamp, A. Guemes, Elimination of temperature effects on damage detection within a smart structure concept, Structural Health Monitoring (2003) 15–17.

[53] M. Zhu, F. McKenna, M. H. Scott, Openseespy: Python library for the opensees finite element framework, SoftwareX 7 (2018) 6–11. doi:https://doi.org/10.1016/j.softx.2017.10.009.

[54] B. Greiner, Operational modal analysis and its application for SOFIA telescope assembly vibration measurements, Universität Stuttgart, Institut für Raumfahrtsysteme, 2009, ph.D. thesis.

[55] E. B. Groth, T. G. R. Clarke, G. Schumacher da Silva, I. Iturrioz, G. Lacidogna, The elastic wave propagation in rectangular waveguide structure: Determination of dispersion curves and their application in nondestructive techniques, Applied Sciences 10 (12) (2020). doi:10.3390/app10124401.

[56] S. Hassani, F. Shadan, Using incomplete frf measurements for damage detection of structures with closely-spaced eigenvalues, Measurement 188 (2022) 110388.

[57] S.-K. Au, J. M. Brownjohn, B. Li, A. Raby, Understanding and managing identification uncertainty of close modes in operational modal analysis, Mechanical Systems and Signal Processing 147 (2021) 107018.

[58] R. Brincker, M. Lopez-Aenlle, Mode shape sensitivity of two closely spaced eigenvalues, Journal of Sound and Vibration 334 (2015) 377–387.

[59] R. Brincker, C. Ventura, P. Andersen, Damping estimation by frequency domain decomposition, in: Proceedings of IMAC 19, Society for Experimental Mechanics, United States, 2001, pp. 698–703, null ; Conference date: 05-02-2001 Through 08-02-2001.

[60] B. Peeters, G. D. Roeck, Reference based stochastic subspace identification in civil engineering, Inverse Problems in Engineering 8 (1) (2000) 47–74. doi:10.1080/174159700088027718.

[61] D. P. Pasca, A. Aloisio, M. M. Rosso, S. Sotiropoulos, Pyoma and pyoma_gui: A python module and software for operational modal analysis, SoftwareX 20 (2022) 101216.

[62] R. Ceravolo, G. De Lucia, E. Matta, A. Quattrone, L. Zanotti Fragonara, Equivalent modal parameters in monitored buildings during the recent italian seismic events, Equivalent modal parameters in monitored buildings during the recent Italian seismic events (2017) 21–30.

[63] K. Zhou, Q.-S. Li, Modal identification of high-rise buildings under earthquake excitations via an improved subspace methodology, Journal of Building Engineering 52 (2022) 104373.

[64] A. Dasar, H. Hamada, Y. Sagawa, D. Yamamoto, Deterioration progress and performance reduction of 40-year-old reinforced concrete beams in natural corrosion environments, Construction and Building Materials 149 (2017) 690–704.

[65] C. Fu, N. Jin, H. Ye, X. Jin, W. Dai, Corrosion characteristics of a 4-year naturally corroded reinforced concrete beam with load-induced transverse cracks, Corrosion Science 117 (2017) 11–23.

[66] K. Kreislova, H. Geiplova, Evaluation of corrosion protection of steel bridges, Procedia Engineering 40 (2012) 229–234.

[67] V. H. Dang, R. Francois, Influence of long-term corrosion in chloride environment on mechanical behaviour of rc beam, Engineering Structures 48 (2013) 558–568.

[68] C. C. Aggarwal, Neural Networks and Deep Learning, Springer, 2018. doi:10.1007/978-3-319-94463-0.

[69] S. Raschka, Python Machine Learning, Packt Publishing - ebooks Account, 2015.

[70] A. Géron, Hands-on machine learning with Scikit-Learn and TensorFlow : concepts, tools, and techniques to build intelligent systems, O'Reilly Media, Sebastopol, CA, 2017.

[71] E. Charniak, Introduction to Deep Learning, The MIT Press, 2019.

[72] I. J. Goodfellow, Y. Bengio, A. Courville, Deep Learning, MIT Press, Cambridge, MA, USA, 2016.

[73] N. Navabian, Development of an automated structural health monitoring system based on wireless sensor network for civil structures, Ph.D. thesis, Auckland University of Technology (2020).

[74] M. Friswell, J. E. Mottershead, Finite element model updating in structural dynamics, Vol. 38, Springer Science & Business Media, 2013.

[75] K. F. Graff, Wave motion in elastic solids, Courier Corporation, 2012.

[76] A. Carpinteri, Advanced structural mechanics, CRC Press, 2017.